Review

# Multi-functional Hollow Structures for Intelligent Drug Delivery

HOU Ping[1,2,3], YANG Nailiang[1,2,3]✉ and WANG Dan[1,2,3]✉

Received April 4, 2024
Accepted May 9, 2024
© Jilin University, The Editorial Department of Chemical Research in Chinese Universities and Springer-Verlag GmbH

Multi-fountional hollow structures have emerged as promising platforms for intelligent drug delivery due to their unique properties, such as high loading capacities and programmed drug release. In particular, hollow multishell structures (HoMSs) with multilevel shell and space can regulate the molecular-level interaction between drugs and materials, so as to achieve the temporal-spatial order and sequential release of drugs. The anisotropic hollow structures can control the drug diffusion process by inducing the macroscopic interface flow through autonomous movement, realizing the targeted drug transport and release. In this paper, a key focus will be HoMSs with their temporal-ordered architectures and anisotropic hollow carriers with directional movement. Their synthesis mechanisms, structure-property relationships, smartly programmed drug delivery and biomedical applications will be discussed, providing insights into designing next-generation intelligent drug carriers.

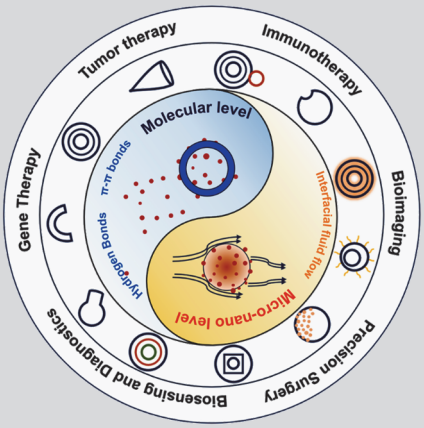


**Keywords** Hollow multishell structure; Anisotropic hollow structure; Intelligent drug carrier; Temporal-spatial order; Directional movement

## 1 Introduction

Intelligent drug delivery systems have become increasingly important for improving therapeutic outcomes. In recent years, significant progress has been made in developing smart drug carriers that can intelligently release drugs through their own structures or in response to specific microenvironmental changes.[1,2] Hollow nanostructures have emerged as one of the most promising platforms for drug delivery owing to their unique properties, such as high loading capacity and interior space for encapsulating molecules.[3−5] Their porous shells can protect drug payloads and control release kinetics. Early research mainly focused on developing single-shelled hollow carriers. Representative examples include liposomes and hollow silica nanoparticles.[5] Liposomes composed of natural or synthetic phospholipid bilayers possess excellent biodegradability and low toxicity.[6] The amphiphilic structure can encapsulate both hydrophilic and hydrophobic drugs but facing the challenge in stability. Hollow silica nanoparticles are attractive due to their customizable mesoporous structures, large surface areas, excellent biocompatibility, and ease of surface functionalization.[7,8] Drugs can be loaded into the porous shells or interior voids. Enzyme and photosensitizer co-encapsulated hollow mesoporous silica nanoparticles modified with pH-responsive surface showed enhanced retention responding to the acidic tumor microenvironment, enhancing therapeutic efficacy against cancer both *in vitro* and *in vivo*.[9] While demonstrating advantages over other carriers, their abilities to achieve precise control over drug release and targetability remained limited.

With growing demands for personalized and precision medicine, more sophisticated carriers are needed. At the molecular level, controlling the interaction forces between drug molecules and carriers can regulate the release process of drug molecules, providing an effective route to achieve controllable drug transportation. On the molecular scale, drug molecules are typically attached to material surfaces through van der Waals forces, electrostatic interaction, hydrogen bonds, $\pi$-$\pi$ bonds and so on.[10,11] By modulating the surface characteristics and structure of the carrier shell, the interaction forces between the shell and drugs can be regulated, thereby controlling drug release behavior. The

✉ YANG Nailiang
nlyang@ipe.ac.cn
✉ WANG Dan
danwang@ipe.ac.cn
1. State Key Laboratory of Biochemical Engineering, Institute of Process Engineering, Chinese Academy of Sciences, Beijing 100190, P. R. China;
2. School of Chemical Engineering, University of Chinese Academy of Sciences, Beijing 100049, P. R. China;
3. Key Laboratory of Biopharmaceutical Preparation and Delivery, Chinese Academy of Sciences, Beijing 100049, P. R. China


https://doi.org/10.1007/s40242-024-4082-9

construction of more shells is also conducive to the formation of different forces between the shell and drugs on multi-surfaces. Hollow multishell structure (HoMS), which contains a minimum of two concentric shells that encapsulate inner voids or chambers, has attracted significant attention.[12−18] Compared to single-shelled hollow carriers, their ordered, multi-layered architectures enable larger drug payloads, better protection of loaded drugs, and sequential release from the innermost to outermost shells. Their unique, multilayered architecture facilitates sequential and sustained drug release through interaction modulation between drug molecules and carrier shells in response to external force. Such hollow multilayer structures hold great potential for co-delivery of multiple therapeutics and achieving synergistic or combinatorial treatment effects through orderly release kinetics.

While comes to the micro-nano scale, when subjected to external forces, the fluid velocity at the solid-liquid interface of hollow carriers will increase, leading to a decrease in the thickness of the fixed diffusion layer and accelerated drug release kinetics according to the Nernst boundary layer theory[19,20] and Fick's diffusion law.[21,22] Therefore, constructing asymmetric fields that generate fluid flow and material motion provides a means to control drug transport behaviors.[23] Anisotropic hollow structures can achieve directional autonomous movement through chemical reactions or external fields, such as light and ultrasound to achieve responsive drug release.[24−26] More importantly, the directional motion of anisotropic hollow structures enhances their ability to overcome biological barriers, and the direction of movement can be adjusted by sensing the specific environment, so as to achieve the targeted transport and the release of drugs. This provides a promising approach for the development of intelligent drug delivery systems with finer control.

In this review, we aim to summarize recent advances in developing multifunctional inorganic hollow nanostructures for intelligent drug delivery (Fig. 1). The key focus will be

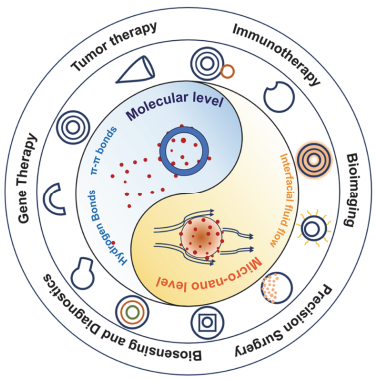


**Fig. 1 Multifunctional hollow structure designed based on the regulation of molecular and micro-nano scale forces for intelligent drug delivery**

HoMSs with their temporal-ordered architectures and anisotropic hollow carriers with directional movement. Their synthesis mechanisms, structure-property relationships, smartly programmed drug delivery and biomedical applications will be discussed. It is hoped that this review provides insights into designing next-generation smart drug carriers through the engineering of hollow nanostructure compositions and architectures.

## 2 HoMS Induced Smart Drug Release

### 2.1 Synthesis of HoMS

The synthesis of HoMS has been an attractive area of research since its discovery in 2004.[27] A major breakthrough was the development of the Sequential Templating Approach (STA) in 2009 by Wang's group,[28] which established a general methodology for the controlled fabrication of HoMS. The key mechanism of STA involves using a sacrificial template rich in precursors that undergoes gradual shell formation during template removal, as shown in Fig. 2A.[12] A wide variety of templates can be utilized, including carbonaceous microspheres, polymers, metal-organic frameworks and nanofibers. The template acts as a "reservoir" to absorb metal or non-metal precursors through various methods, such as sol-gel, ion exchange and hydrothermal processes. This allows for homogeneous or heterogeneous precursors to infiltrate both the surface and interior of the template to achieve a large penetration depth, which is crucial for multilayer shell growth. Then template removal is carried out, influenced by both thermodynamic and kinetic factors. During removal, shell formation occurs through the dehydration, aggregation, and crystallization of precursors. Repeated formation and detachment of shells lead to the creation of multishell structures and internal cavities.

Numerous studies have provided insights into the effects of various experimental parameters. The properties of templates, such as their composition, surface functionality, and charge distribution determine how precursors are distributed within them.[29] The rates of shell formation ($R_{sf}$) and template removal ($R_{tr}$) also exert a profound influence through their competitive relationship, as described in Fig. 2B.[28] These rates are influenced by oxygen diffusion and template reaction kinetics, respectively. For example, in the case that Co ion has a catalytic combustion effect, $R_{tr}$ plays a leading role in the formation of Co-based HoMS. By doping Mn ions in the matrix, the dehydration and crystallization rates of spinel $Co_3O_4$ can be changed, leading to the change of $R_{sf}$. Therefore, the competitive effect between $R_{sf}$ and $R_{tr}$ can be regulated by controlling the amounts of Mn precursors, resulting in the successful preparation of septuple-shelled $(Co_{2/3}Mn_{1/3})(Co_{5/6}Mn_{1/6})_2O_4$ HoMS


https://doi.org/10.1007/s40242-024-4082-9

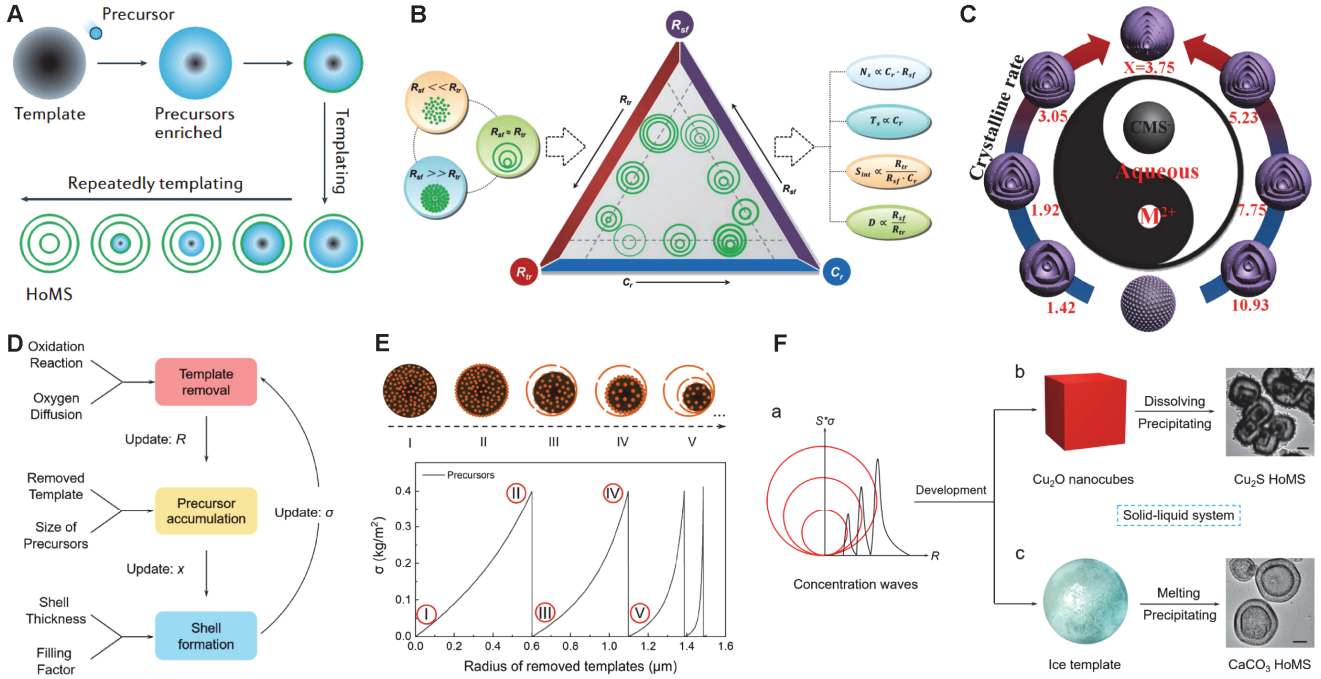


**Fig. 2 Prepration of HoMS *via* STA (A), illustration of the intercorrelations among the key parameters of STA (B), septuple-shelled hollow microspheres synthesized by finely controlling the molar ratio of Co/Mn using STA (C), structure of the mathematic model for the formation of HoMS (D), variation of the *σ* during the template removal process and the schematic illustrations of labeled states (E), and illustration of the relationship between concentration waves and the as-formed HoMS (F)**

(A) Reprinted with permission from Ref. [12], Copyright 2020, Springer Nature; (B) reprinted with permission from Ref. [28], Copyright 2018, Wiley-VCH; (C) reprinted with permission from Ref. [31], Copyright 2017, Wiley-VCH; (D—F) reprinted with permission from Ref. [40], Copyright 2023, Wiley-VCH.

(Fig. 2C).[30,31] Factors like precursor concentration, absorption time, calcination temperature and heating rate have been shown to impact shell morphology. By analyzing these and other factors, the number of shells, shell thickness, and inter-shell spacing can be precisely regulated.[32—35] The composition, structure and properties of the as-prepared HoMS can be further tuned by phosphating, vulcanization, doping or surface functionalization.[36—39]

Mathematical modeling and numerical simulation further elucidate the physical essence of HoMS formation *via* the STA (Fig. 2D).[40] Physical models are first abstracted from experimental processes, depicting the evolution of sequential templates and the accumulation of precursors on their surfaces. Crucially, numerical solutions reveal the surface concentration of precursors ($\sigma$) exhibits periodic concentration waves, as shown in Fig. 2E. This phenomenon provides insights into the mechanism: shell structures represent the concrete manifestation of such concentration waves. The number and spacing of shells directly correlate with the amplitude and frequency of the concentration waves. By establishing equilibrium between $R_{sf}$ and $R_{tr}$, simulations have demonstrated the controlled fabrication of various HoMS. It also allows HoMS fabrication, such as $CaCO_3$ at low-temperature (Fig. 2F), offering opportunities to precisely engineer structures for bio-related applications.

## 2.2 Temporal-spatial Ordering Property of HoMS for Program Drug Delivery

HoMS has attracted significant interest as drug carriers due to their unique geometric structures consisting of multiple concentric shells with inner voids. Compared to single-shelled carriers, HoMS enables temporal-spatial control over drug loading and releasing through the separate shells and pores. Drugs can be encapsulated at distinct sites within the HoMS structure and released in a prescribed temporal sequence following diffusion pathways. The sequential drug loading process occurs as molecules diffuse from the outer shell inwards (Fig. 3A).[41,42] Different drugs can be encapsulated using different loading mechanisms according to their physicochemical properties. Chemical bonds, such as disulfide bonds and hydrazone bonds allow drugs to be conjugated onto the carrier for stable encapsulation. Pore size and surface properties of each shell determine the diffusion rate and loading capacity for different drug molecules. Through computational modeling, Ma *et al.*[43] revealed the loading process of drugs by multishelled hollow carbonate nanospheres involves three steps,

including the fast surface adsorption stage, slow adsorption stage, and gradual equilibration stage. First, the drug is attached to the shell surface through hydrogen bonding, reducing the gap and increasing the capillary force. When drug loading over 24 h, the loading of drug molecules is dominated by π-π stacking. The multi-step process allows drugs of varying properties to be compartmentalized at distinct sites within the hollow multishelled structures, as shown in Fig. 3A.

The spatial separation of drugs loaded in different shells under various interactions endows HoMS the ability to release drugs in a predetermined order. With multiple shells, well-separated sites exist for temporally and spatially ordered drug release regimens. This overcomes limitations of single drug carriers and enables more effective combination therapies. Release typically occurs in three stages dictated by the spatial distribution of the drug within the structure, as described in Fig. 3B.[44] Drugs physically adsorbed on the outer shell surfaces are initially released in a burst manner. This rapid desorption of outer surface-loaded drugs constitutes the first stage of release from HoMS. The second stage involves sustained release of drug molecules residing within the internal cavities of HoMS. The porous shells allow for gradual diffusion-controlled transport of encapsulated drugs out of the carrier structure. Stimulus-responsive release stage may also be achieved depending on the interactions between drug molecules and shell surfaces. Hydrogen bonding or other interactions can reversibly bind drugs to shells, enabling their detachment to be triggered in response to external stimuli like pH changes. Crucially, the release rate can be precisely tuned. Smaller pore sizes and thicker shells prolong diffusion pathways, slowing release kinetics over hours to days for effective dosing.[45,46] Inter-shell interactions, such as hydrogen bonding and π-π stacking further retard drug mobility.

Stimuli-responsiveness adds an additional dimension of control. Changes in environmental cues like pH, redox potential and enzyme concentrations trigger accelerated release from "hidden" drug reservoirs.[47,48] For example, Zhao *et al*.[49] developed polyethylene glycol modified $TiO_2$ HoMSs ($TiO_2$ HoMS@PEG) that maintained steady antibiotic release until additional pathogens were added, at which point drug concentrations surged to combat the infection. By incorporating multiple independent or synergistic stimuli-responsive shells, dynamic dosage profiles can be achieved.[50−52] Under physiological conditions, drugs remain securely encapsulated until the system encounters diseased tissue microenvironments (*e.g.*, acidic tumor or inflammatory pH).[53] This allows preferential accumulation and "activatable" release at target sites, minimizing side effects.

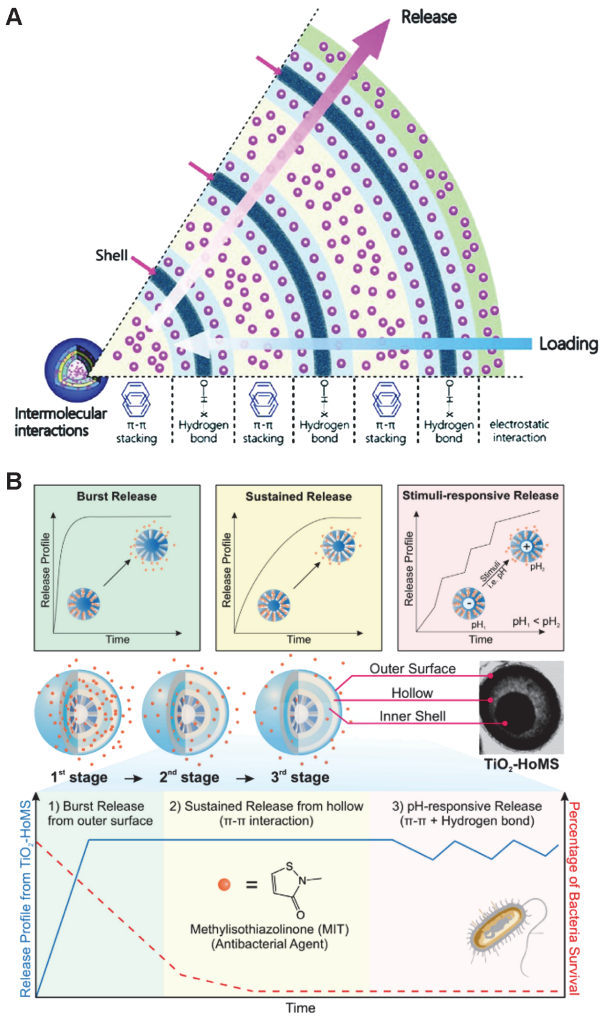


**Fig. 3 Drug interaction and release behavior with HoMS (A), and drug release patterns of HoMSs including burst, sustained, and stimulus-responsive drug release modes (TEM shows typical $TiO_2$ HoMS) (B)**

(A) Reprinted with permission from Ref. [42], Copyright 2023, the Royal Society of Chemistry; (B) reprinted with permission from Ref. [44], Copyright 2020, Elsevier.

## 2.3 Structurally Induced Sequential Release of HoMS

HoMS have emerged as a promising intelligent drug delivery platform owing to their unique structural properties enabling precise spatiotemporal control over drug release. Considerable research efforts have focused on utilizing the multi-dimensional release capabilities of HoMS for various biomedical applications. $TiO_2$ HoMS have been developed for the sequential release of antibiotics and antibacterial agents to combat drug-resistant infections more effectively. Zhao *et al*.[49,54] introduced the broad-spectrum antimicrobial agent MIT into $TiO_2$ HoMS and found that the antibacterial effect increased with the increase of shell number. The inhibitory effect of 3s-$TiO_2$-HoMS on the growth of *Escherichia coli* exceeded 400 h, superior to hollow


https://doi.org/10.1007/s40242-024-4082-9

spheres and 2s-$TiO_2$-HoMS (Fig. 4, A and B). In particular, 3s-$TiO_2$-HoMS sterilizes the environment eight times longer than the free antibacterial agent. More importantly, HoMSs provide a dynamic, responsive release mechanism triggered by environmental changes. When additional pathogens are added to the environment, the HoMS can further release stored drugs (Fig. 4C). This phenomenon is attributed to the adsorption changes of different spatial components and the physical barrier of the multilayer shell, which allows the drugs to be released in different states from different adsorption sites under pathogen stimulation. The results show that multiphase release is required for drug delivery in bacterial infections, and HoMSs exhibit good multiphase release, thus providing strategies for designing dynamic and intelligent microenvironment-responsive drug delivery.

Modifications to HoMS carriers provide opportunities to further optimize controlled release behavior. For example, surface functionalization of shells with polymers like PEG introduces stimuli-responsive gates (Fig. 4D).[54] The interaction between the PEG-functionalized shell and the drug molecule is controlled by the environmental pH value, thus providing the pH response switch and rate regulator function for $TiO_2$ HoMS. Specifically, in a neutral environment with a pH of 7, the release of cassone is hindered, while when the pH drops to 4, the release efficiency of cassone is significantly improved (Fig. 4, E and F). Changes in the water environment greatly affect the mass transfer behavior within HoMS, thereby re-establishing the balance. In addition, the dynamic interaction caused by changes in the microenvironment reflects the mutual coordination of two different dominant mechanisms in competition, which further demonstrates the controllability of HoMS mass transfer performance. Such controlled long-term release profiles open up new avenues for the development of novel long-lasting antibacterial materials with intelligent stimulus-responsive behavior.

HoMS can effectively load poorly water-soluble anticancer drugs inside hollow cavities or in porous shells, improving cancer chemotherapy by enhancing drug solubility/stability and reducing side effects. Hao *et al*.[55] prepared a hierarchical walnut kernel-like mesoporous silica nanomaterial (WMSN) as a drug carrier for cancer therapy. The doxorubicin (DOX) loading capacity was up to 367.4 mg/g, demonstrating the superior capacity of hierarchical nanocarriers. Encapsulation protects drugs from degradation and prevents nonspecific interactions, allowing intravenous administration of insoluble compounds. *In vivo* studies show WMSN can be effectively taken up by cells to improve drug utilization (Fig. 5A). Under acidic conditions (pH 4.5), DOX can achieve effective release from the multishell structure due to the reduction of hydrogen bond density, which significantly enhances the toxic killing effect on tumor cells compared with free DOX (Fig. 5B). Ma *et al*.[56] prepared a variety of hierarchically porous triple-shelled

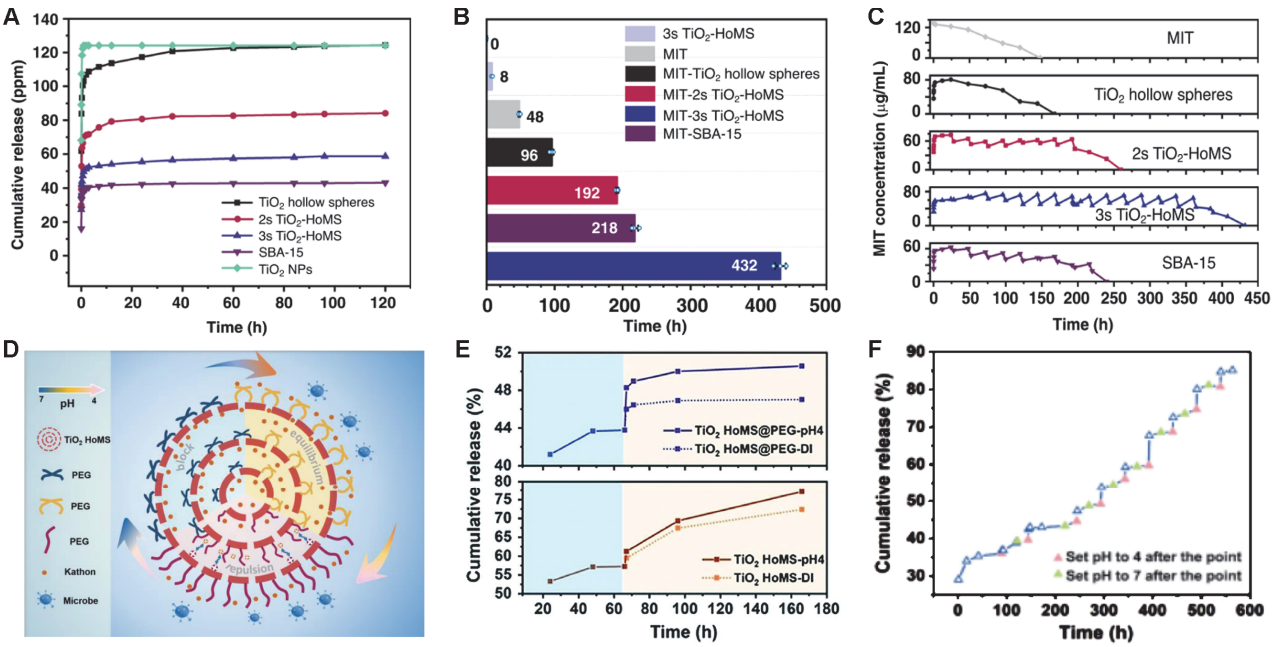


**Fig. 4 Cumulative release performance of MIT in HoMS (A), sterile maintenance performance under different conditions with the same MIT amount (B), bacterial-responsive release profiles of different samples (C), schematic illustration of the pH-responsive antimicrobial release mechanism of $TiO_2$ HoMS@PEG (D), pH-responsive release performance of 3s-$TiO_2$ HoMS and 3s-$TiO_2$ HoMS@PEG (E), and recyclable pH-responsive release performance of 3s-$TiO_2$ HoMS@PEG (F)**

(A—C) Reprinted with permission from Ref. [49], Copyright 2020, Springer Nature; (D—F) reprinted with permission from Ref. [54], Copyright 2022, Wiley-VCH.


https://doi.org/10.1007/s40242-024-4082-9

hollow $La_2(CO_3)_3$, $CaCO_3$ and $BaCO_3$ (Fig. 5C). Hollow multishell $CaCO_3$ has the characteristics of high drug loading capacity and sustained drug release. *In vivo* results showed that intratumoral administration of multi-shelled $CaCO_3$ with DOX loading had a significantly better tumor reduction effect than free DOX, indicating the potential application of HoMS as a new drug delivery platform in targeted cancer therapy. Sun *et al.*[41] have prepared multifunctional multi-shelled hollow nanospheres ($a_m$-ZnO@CuO@Au HNSs) with DOX and RGD peptide-conjugated (Fig. 5D), which can target and kill cancer cells by $Zn^{2+}/Cu^{2+}$ therapy, chemotherapy, and phototherapy. Functionalization of hollow structures with targeting ligands like folic acid (FA) can further improve tumor selectivity.[57,58] Zhou *et al.*[59] developed lignin-assembled hollow $Fe_3O_4$ nanoparticles loaded with DOX. These carriers could be guided to tumor sites using an external magnetic field for active targeting. Such stimuli-responsive targeting and release properties address the limitations of conventional chemotherapy. HoMSs also enable co-delivery of diagnostic and therapeutic agents for real-time treatment monitoring. Huang *et al.*[60] synthesized multi-shelled mesoporous silica nanospheres loaded with both DOX and a near-infrared fluorescent dye (Fig. 5E). In cancer cells, DOX was directionally released into the cytoplasm and nucleus for chemotherapy. Meanwhile, the encapsulated dye remained detectable within cells for long-term imaging, confirming the "theranostic" capabilities of this dual-loaded

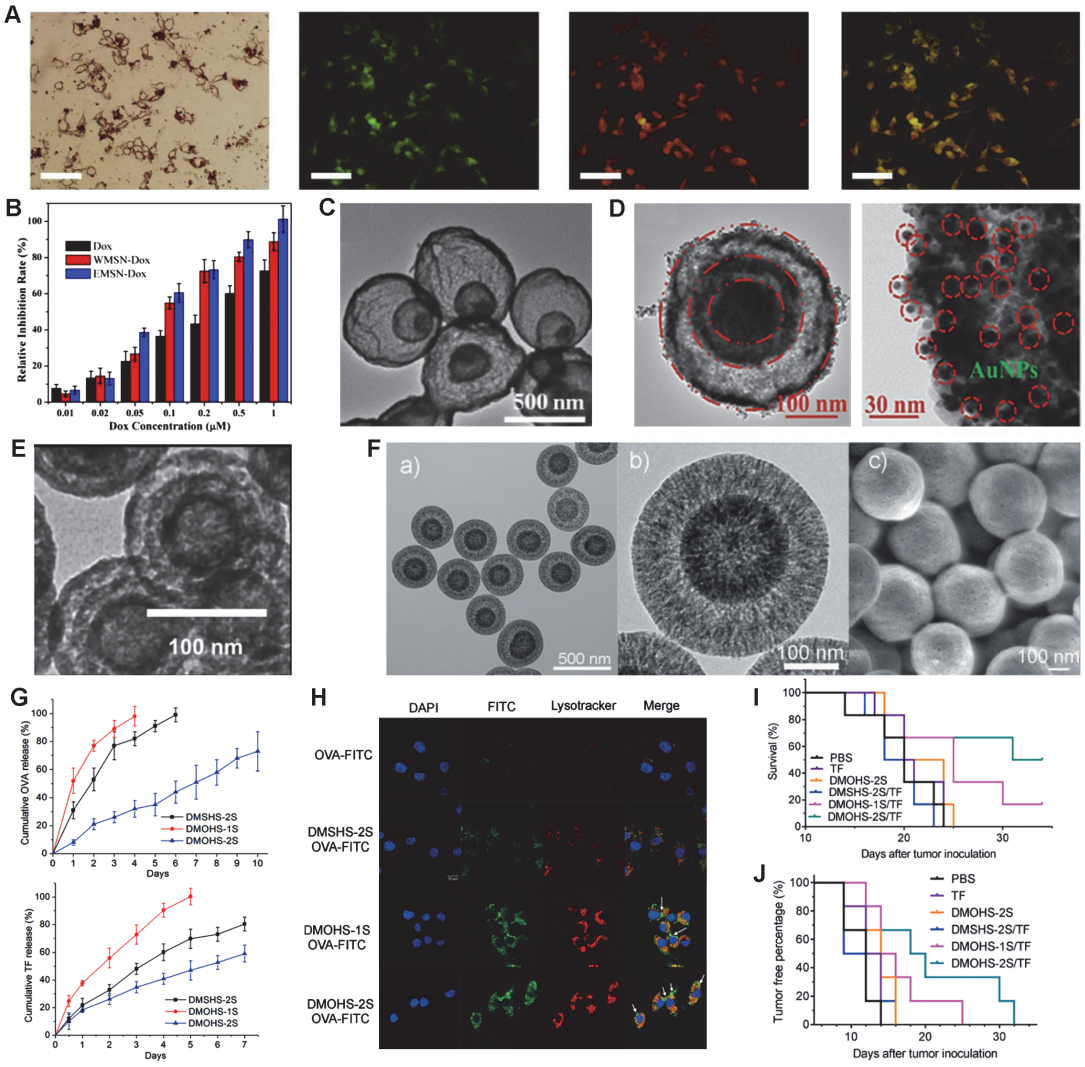


**Fig. 5 Confocal images of SK-BR-3 cells after treating with DOX-loaded FITC-labeled WMSN (scale bars=50 μm) (A), inhibition rates of different samples on SK-BR-3 cells for 24 h (B), TEM image of $BaCO_3$ (C), TEM and HRTEM images of $a_m$-ZnO@CuO@Au HNSs (D), TEM image of triple-shelled silica nanoparticles (E), TEM images (a, b) and SEM image (c) of DMOHS-2S (F), OVA and TF release profile from various nanoparticles in PBS solution (G), confocal images of different samples incubated for 10 h (H), and survival rate (I) and tumor-free percentage (J) of mice after immunization during various vaccine formulations**

(A, B) Reprinted with permission from Ref. [55], Copyright 2018, Elsevier; (C) reprinted with permission from Ref. [56], Copyright 2016, the Royal Society of Chemistry; (D) reprinted with permission from Ref. [41], Copyright 2020, the Royal Society of Chemistry; (E) reprinted with permission from Ref. [60], Copyright 2011, Elsevier; (F—J) reprinted with permission from Ref. [46], Copyright 2017, Wiley-VCH.


https://doi.org/10.1007/s40242-024-4082-9

system. Co-delivery of imaging modalities with HoMS carriers provides a non-invasive means to quantitatively track drug distribution and therapeutic responses *in vivo*.

HoMS can also act as a potent adjuvant to stimulate a strong immune response and improve cancer treatment. Yu *et al*.[46] prepared dendritic mesoporous organosilica with controllable number of shells (DMOHS), as shown in Fig. 5F. When loading ovalbumin (OVA) or B16F10 tumor cell fragments (TF), the double-shelled DMOHS showed the most sustained release profile compared to that of single-shelled one (Fig. 5G). This is attributed to the strong hydrophobic interaction between DMOHS-2S and the antigen, as well as the presence of a bivalve structure, which can act as an effective barrier to slow the diffusion of protein molecules. OVA-FITC-loaded DMSHS-2S showed enhanced cellular uptake and a certain degree of endo/lysosome escape compared to proteins alone (Fig. 5H). Moreover, silicon-based vaccine preparations showed significantly improved tumor inhibition. Compared with the other groups, DMOHS-2S immunized mice had significantly longer survival, with a survival rate of 50% after 35 days of tumor inoculation (Fig. 5I). In addition, the DMOHS-2S vaccine formulation effectively prolonged the tumor-free rate in the mice, significantly delaying tumor growth to 31 days, while all other groups developed tumors 100% within 25 days (Fig. 5J). These results indicate that both the composition and double-shell structure of rich organic silica are conducive to enhancing the adjuvant effect *in vivo*.

## 3 Anisotropic Hollow Structures Induced Smart Drug Delivery

### 3.1 Synthesis of Anisotropic Hollow Structures

Based on the diverse sizes and shapes, the anisotropic hollow structures are often divided into three categories: hollow spheres with an opening, hollow stomatocytes and flask-shaped hollow spheres.[61−64] Templating method has proven to be an effective method to construct anisotropic hollow sphere with an opening. Xia *et al*.[65] utilized a template-directed synthesis method to create silica nanocapsules featuring precisely defined openings (Fig. 6A). By employing Au-polystyrene (PS) Janus particles as templates, the hydrophobic precursor selectively formed a vinyl silica shell on the hydrophobic PS regions, avoiding the hydrophilic Au surfaces. The subsequent removal of gold nanoparticles and PS beads through etching and calcination, respectively, resulted in the formation of vinyl silica nanoparticles with a pore in the wall. Notably, the size of these openings could be adjusted from 24 nm to 62 nm by varying the diameter of the Au nanoparticles from 50 nm to 100 nm. PS spheres also served as templates for constructing anisotropic hollow structures by growing an $SiO_2$ shell. These structures were then endowed with self-propulsion capabilities through surface modification with enzymes (Fig. 6B).[66] Kwon *et al*.[67] advanced this field by synthesizing Au/Pt-egg-in-nest (Au/Pt-EN) nanostructures with an average diameter of 62 nm, using a dynamic silica yolk-shell as the template (Fig. 6C). Through Ostwald ripening process, a large Au seed was installed within the silica template, and then seed-mediated growth of surfactant-free Pt nanodendrites was conducted, followed by the etching of $SiO_2$-cast, resulting in the unique anisotropic nest-like Pt-structure with the Au seed embedded at the closed bottom. Owing to the distinctive Janus nestlike hollow nanoarchitectures, the Au/Pt-ENs demonstrated a remarkable capability to overcome random Brownian motion, exhibiting life-like directional movements. Feng *et al*.[68] employed $MnO_2$ microspheres as templates to grow zirconium-based coordination polymer (Zr-CP)/metal-organic framework structures, achieving a hollow-shell structure, which can produce $O_2$ bubbles to achieve autonomous motion with $H_2O_2$ as the fuel (Fig. 6D). This templating principle has also been applied to fabricating the open-mouthed noble metal (Au and Pt) hollow structures (Fig. 6E),[69] hollow $SiO_2$ microspheres with an opening,[70] PS with an opening[71], hollow polydopamine, single-holed cobalt/N-doped carbon (Co/NC) hollow particles,[72] and single-holed hollow poly(ethyleneglycol)dimethacrylate nanospheres.[73]

Additionally, hollow PS particles with a single opening in the surface have been achieved by swelling polymer spheres with an organic solvent, followed by a freeze-drying process, shown in Fig. 6F.[74] This process allows for the control of the opening diameter from 50 nm to 224 nm by adjusting factors, such as solvent selection, freezing/evaporation conditions, and temperature. Chu *et al*.[75] explored lignin hollow nanospheres with a pore leveraging the effect of tetrahydrofuran (THF) on the self-assembly behavior of lignin molecules. By fine-tuning the ratio of water to THF, the formation of membranes by lignin molecules at the biphasic interface and the infiltration of water molecules into these membranes are modulated. This adjustment leads to a differential pressure across the membrane, thereby inducing the creation of pores within the shell structure.

Hollow stomatocytes can be transformed from spherical polymersomes in a controlled manner through a process of dialysis (Fig. 7A).[76,77] The aperture size of these stomatocyte formations can be meticulously adjusted by altering the proportion of THF used for polymer dissolution, as depicted in Fig. 7B.[78] During the transition from the flexible to the glassy state, platinum nanoparticles (Pt NPs) differing in size from 30 nm to 150 nm were engulfed inside the stomatocyte pockets (Fig. 7C).[79] By altering the size of the platinum

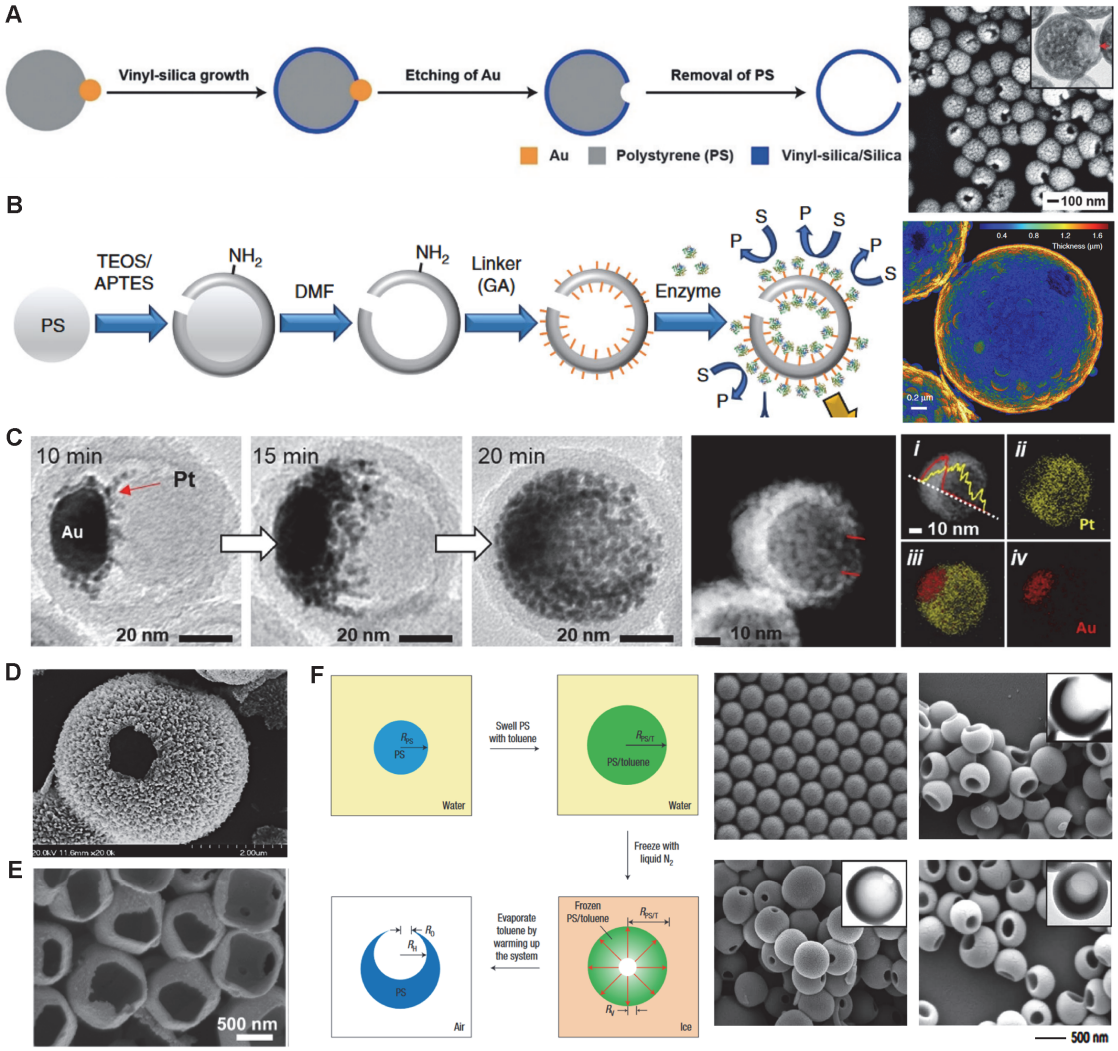


**Fig. 6 Schematic showing the synthesis of hollow silica spheres with a well-defined hole in the wall with TEM image of hollow silica spheres synthesized with 100 nm Au nanoparticles as the initial seeds for PS growth (A), fabrication diagram and false color TEM image of hollow silica micromotors (B), time course TEM images of growth of Pt dendrites from Au seeds with HAADF STEM images, EDX elemental mappings and line profiles of Au/Pt-ENs (C), TEM image of hollow Zr-CP (D), TEM image of open-mouthed noble metal hollow structures (E), and synthesis of hollow PS nanostructures through swelling and subsequently freeze-drying with SEM and TEM images of PS solid spheres and PS nanostructures with different opening sizes (F)**

(A) Reprinted with permission from Ref. [65], Copyright 2019, Wiley-VCH; (B) reprinted with permission from Ref. [66], Copyright 2019, Springer Nature; (C) reprinted with permission from Ref. [67], Copyright 2021, Wiley-VCH; (D) reprinted with permission from Ref. [68], Copyright 2018, American Chemical Society; (E) reprinted with permission from Ref. [69], Copyright 2015, American Chemical Society; (F) reprinted with permission from Ref. [74], Copyright 2005, Springer Nature.

nanoparticles, the quantity of encapsulation can be controlled, enabling the composite structure to achieve directional motion in $H_2O_2$ environments. This submicron-scale stomatocyte architecture has inspired further research focusing on the functionality of nanomotors.[80−85] By incorporating magnetic nanoparticles within their cavities, the trajectory of the stomatocyte nanomotors can be manipulated using a magnetic field.[86] With the *in-situ* grown $CaCO_3$ nanoparticles, the supramolecular assembly-based stomatocytes are activated in slightly acidic pH showcasing "pH taxis" towards tumor cells without the need for any sophisticated/complicated technologies or an external fuel source.[87] Hest *et al*.[88] modified polymer stomatocytes with a cell membrane isolated from erythrocytes to ensure that the surface characteristics matched those of red blood cells, which exhibited long circulation times in mice (Fig. 7D). Leveraging the lower critical solution temperature (LCST) property, poly(*N*-iso-propyl acrylamide) (PNIPAM) has been chemically grafted onto the stomatocyte nanomotors, acting as a thermosensitive gate to modulate speed (Fig. 7E).[89] By thermally controlling the collapse of PNIPAM brush, the entry points of the stomatocyte nanomotors can be thermally modulated, thereby regulating the influx of hydrogen


https://doi.org/10.1007/s40242-024-4082-9

peroxide fuel to control their motility. By selectively reducing azide compounds on the outer surface of poly(ethylene glycol)-b-poly(*D*,*L*-lactide) (PEG-PDLLA) stomatocytes, different functionalities can be achieved on the internal and external surfaces, allowing for the loading of fluorophores and other molecules on the outside, while enzymes are encapsulated on the inner surface to induce motion in the presence of fuel (Fig. 7F).[90] Moreover, dimpled PS microparticles have been prepared in a dispersion polymerization process.[91] Further dispersing them in a water-toluene mixture followed by evaporating the solvent at room temperature results in the formation of hollow PS spheres with a single opening (Fig. 7G).[92] A similar method can also be applied to the preparation of hollow concave Zn doped $Co_3O_4$/C composites.[93]

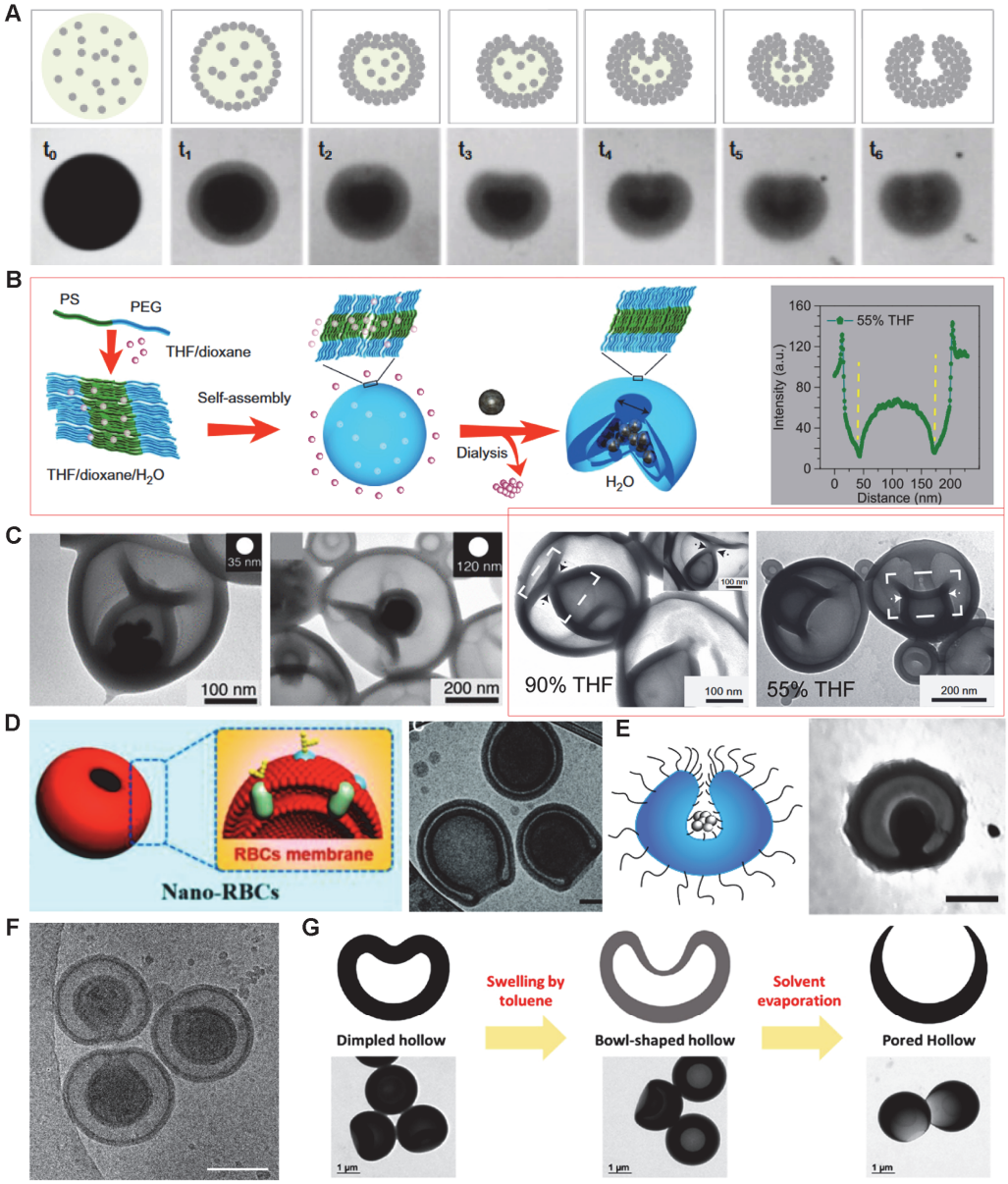


**Fig. 7 Schematic illustrations and bright-field microscopic images of the forming process of the stomatocyte photonic crystal barcodes (A), strategy for the selective and controlled entrapment of Pt NPs inside the stomatocytes during shape transformation (B), hollow stomatocytes encapsulated of Pt NPs of 35 nm and 120 nm (C), schematic illustration of the fabrication of biodegradable stomatocytes and its TEM image (scale bar=100 nm) (D), schematic representation and TEM image of the Pt NP-loaded stomatocyte (scale bar=200 nm) (E), cryo-TEM picture of PEG-PDLLA stomatocytes (scale bar=250 nm) (F), and formation of hollow PS particles from presynthesized hollow and dimpled PS seeds during the swelling and evaporation processes (G)**

(A) Reprinted with permission from Ref. [77], Copyright 2019, Oxford University Press; (B) reprinted with permission from Ref. [78], Copyright 2012, Springer Nature; (C) reprinted with permission from Ref. [79], Copyright 2012, American Chemical Society; (D) reprinted with permission from Ref. [88], Copyright 2019, Wiley-VCH; (E) reprinted with permission from Ref. [89], Copyright 2016, Spring Nature; (F) reprinted with permission from Ref. [90], Copyright 2019, Spring Nature; (G) reprinted with permission from Ref. [92], Copyright 2019, American Chemical Society.


https://doi.org/10.1007/s40242-024-4082-9

Flask-shaped hollow silica nanoparticles have been successfully crafted by anisotropic sol-gel growth in a water/*n*-pentanol emulsion.[94] As shown in Fig. 8A, the process entails hydrolyzed (3-chloropropyl)trimethoxysilane (CPTMS) organizing at the water-oil boundary, followed by selective hydrolyzed tetrabutylorthosilicate (TBOS) deposition, creating a thin silica layer. By expanding the silica shell, aqueous solution was gradually extruded out of the droplet to form the bottle neck and opening of the nanobottles. The silica nanobottles with an average diameter of 350 nm and an opening of 100 nm possess a hydrophobic exterior surface and a hydrophilic interior (Fig. 8B). The internal loading of hydrophilic Pt NPs within these nano-flasks rendered these nano-flasks effective nanomotors through the catalytic breakdown of $H_2O_2$. By further self-assembling monolayers of $Fe_3O_4$ nanoparticles and mesoporous silica layers on the surface of hollow silica nanobottles, it has been proven to achieve both magnetically induced precise directional control and speed regulation induced by catalase-like enzymatic activity (Fig. 8C).[95] The neck of nanobottles can be regulated by changing the amount of TEOS.[96] Chen *et al*.[97] fabricated novel asymmetric hollow carbonaceous nanoflasks using a soft template method. As shown in Fig. 8D, sodium oleate and P123 were employed as double soft templates to hydrothermally direct the polymerization of ribose under acidic conditions. Through subtle synergistic interactions between the templates and biomass precursor, hollow carbonaceous shells with openings were formed. The carbon nanobottles can be further modified with noble metals or enzymes to enable self-propulsion and chemotaxis in various biofuels.[98,99] The functionality of these silica nano-flasks was also enhanced by showcasing their ability for light-induced self-propulsion, a result of thermal near-infrared (NIR) heating of the internal volume of the nanoflask.[100]

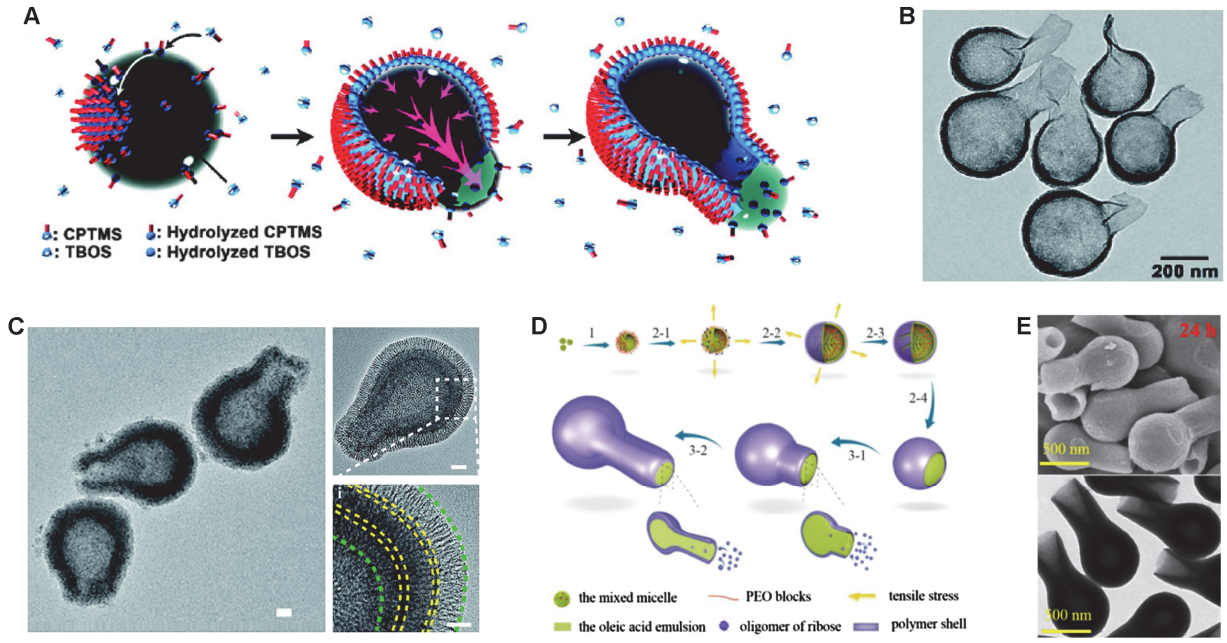


**Fig. 8 Illustration of the formation (A) and TEM image (B) of chemically asymmetric silica nanobottles, TEM images of magnetic mesoporous silica nanobottles (scale bar=50 nm) (C), schematic growth mechanism of the carbon nanovases (D), and TEM and SEM images of carbon nanovases with hydrothermal time of 24 h (E)**

(A, B) Reprinted with permission from Ref. [94], Copyright 2016, Wiley-VCH; (C) reprinted with permission from Ref. [95], Copyright 2021, Wiley-VCH; (D, E) reprinted with permission from Ref. [97], Copyright 2017, American Chemical Society.

## 3.2 Directional Movement in Anisotropic Hollow Particles

Anisotropic hollow structures have attracted increasing attention for intelligent drug delivery, due to the targeted and responsive drug release through autonomous motion. The hollow interiors and asymmetric shapes allow efficient fluid flow and interaction with surrounding media, enabling conversion between various forms of energy for self-propulsion. Currently, chemical propulsion and external physical actuation are two general strategies to power anisotropic hollow particle motility. More specifically, the driving mechanisms can be divided into five types on the basis of different models of propulsion: electrophoretic mechanism, diffusiophoretic mechanism, bubble propulsion and thermophoretic mechanism, and chemotaxis. By utilizing the microenvironment in the organism, or applying an external field, the material motion mechanism can be changed to achieve specific drug delivery behaviors to improve therapeutic efficacy.


https://doi.org/10.1007/s40242-024-4082-9

Self-electrophoresis is an emerging propulsion mechanism for directing the motion of micro/nanomotors. It involves the generation of an electric field at the motor surface through asymmetric redox reactions occurring at different sites. The field then interacts with the mobile ions in the interfacial double layer, inducing an electro-osmotic slip flow that propels the motor. The self-electrophoretic velocity ($v$) can be estimated using the Smoluchowski equation:[101]

$$v = \frac{\varepsilon \zeta E_\infty}{\eta}$$

where $\varepsilon$ is the solution permittivity, $\zeta$ is the zeta potential of the motor, $E_\infty$ is the self-generated electric field, and $\eta$ is the viscosity of the solution. Various motors driven by this mechanism have been demonstrated, including the pioneering $SiO_2$-Pt Janus particles by Wang *et al*.[102] that swim *via* on-board catalysis of $H_2O_2$. The oxidation of $H_2O_2$ at the anode produces protons ($H_2O_2 \longrightarrow O_2+2H^++2e^-$), whereas reduction of $H_2O_2$ at the cathode consumes protons ($H_2O_2+2H^++2e^- \longrightarrow 2H_2O$), leading to a local electric field pointing from the cathode to the anode (Fig. 9A). In turn, this self-generated electric field drives the charged swimmers to migrate electrophoretically at speeds ranging from a few to hundreds microns per second (Fig. 9B). Several factors can influence the effectiveness of self-electrophoretic motors, such as the properties of the surrounding fluid medium including viscosity and ionic strength.[103,104] Strategies to optimize performance involve tuning the zeta potential *via* surface functionalization, increasing the magnitude of electric field produced, and proper selection of motor geometry.[105]

Diffusiophoresis refers to the directed motion of particles induced by concentration gradients of solutes or solvents. The gradient gives rise to an osmotic flow that slips along the particle-fluid interface, propelling the particle at speeds of typically 0.1—10 μm/s. Depending on the nature of the solutes or solvents added, the diffusiophoretic for the directional propulsion can be further divided into ionic diffusiophoresis and nonionic diffusiophoresis, corresponding to electrolyte and nonelectrolyte matters, respectively. When the diffusion motion of the particles was caused by gradients of uncharged (non-electrolyte) solutes, such as $N_2$, $H_2$, and $NH_3$ on the surface of the particles, the velocity of the rigid spherical particle ($U$) assumed locally parallel to the particle surface was described by Anderson *et al*.[106] as:

$$U = \frac{k_B T}{\eta} KL\nabla C$$

where $K$ is the Gibbs' absorption length, $L$ is the length of the solute-surface interaction, $k_B$ is the Boltzmann constant, $T$ is the solution temperature, $\eta$ is the fluid viscosity, and $\nabla C$ is the solute concentration gradient. By considering the osmotic pressure of asymmetrically distributed molecules on the particle, the particle motion due to a mass concentration gradient near the catalytic site can be roughly estimated. If the volume, through which the particle moves is approximately equal to the volume of the particle itself, then the osmotic pressure can be estimated as $p=k_BT/V\approx k_BT/(2R)^3$, and resulting force $F=p\pi R^2$ acts on the particle. This force opposes the viscous resistance $F=6\pi\mu Rv$ on the particle, moving a distance $vt=(\pi/2)a\approx a$, where $\mu$ is the viscosity and $R$ and $v$ are the radius and the velocity of the particle, respectively.[107] For example, polystyrene (PS)/Pt axis-asymmetric hollow bowl-shaped Janus micromotors (HBJMs) catalyze the decomposition of $H_2O_2$ producing difference of the $O_2$ concentration gradients between the Pt side and the PS side molecules, creating localized asymmetry in concentration distribution (Fig. 9C).[108] This generates an osmotic pressure difference that propels the particle, enabling autonomous motion.

When the motion of the particles was caused by gradients of monovalent electrolyte, the speed ($U$) can be approximated by the equation:[109]

$$U = \left[-\frac{\varepsilon\zeta}{4\pi\eta}\frac{k_BT}{e}\left(\frac{D_C - D_A}{D_C + D_A}\right) + \frac{\varepsilon}{2\pi\eta}\left(\frac{k_BT}{e}\right)^2 \ln(1-\varepsilon^2)\right]\frac{\mathrm{d}\ln C}{\mathrm{d}x}$$

where $k_B$ is the Boltzmann constant, $T$ is the temperature, $\eta$ is the viscosity of the solution, $e$ is the charge of an electron, $\mathrm{d}\ln C/\mathrm{d}x$ is the gradient of the electrolyte, $D_C$ is the diffusion coefficient of the cation, $D_A$ is the diffusion coefficient of the anion, $\zeta$ is the zeta potential of the particle surface and $\varepsilon=\tanh[(e\zeta)/(4k_BT)]$. Such gradients can be imposed externally or generated through on-board chemical reactions, enabling autonomous ionic diffusiophoretic motors. Due to the diversity of catalysis, ionic and non-ionic diffusion diffusiophoretic can also occur simultaneously. Wang *et al*.[110] prepared iridium hemispheric layer coated $SiO_2$ Janus micromotors, which can catalyze the decomposition of hydrazine to form neutral ($N_2$, $H_2$, $NH_3$) molecules and a cationic ($NH_4^+$) species as product, resulted from the protonation of $NH_3$ in water (Fig. 9D). There exist both ionic and nonionic diffusiophoretic, and the direction of motion caused by the two is opposite. In the initial stage, it moves towards $SiO_2$ side, indicating that non-ionic diffusiophoretic plays a leading role. As the motor continues to move, more hydrazine reacts, creating additional cations that increase ion diffusion and thus cause the motor speed to gradually decrease over time.

Bubble propulsion is an efficient mechanism for powering the motion of small-scale machines. By harnessing the recoil force upon bubble growth and release, systems of varying geometries can achieve high speeds up to centimeters per second. Bubble propulsion requires the concentration of gas molecules around the surface of particles in the system being high enough to produce bubbles. For example, when the $O_2$ concentration exceeds its


https://doi.org/10.1007/s40242-024-4082-9

critical nucleation concentration of 68 mmol/L, $O_2$ starts to nucleate to form nanobubbles in the cavity. Kong *et al*.[100] fabricated an asymmetric hollow structure by loading platinum nanoparticles onto the surface of a carbon vase. When immersed in $H_2O_2$ solution, both the inner and outer surfaces generate $O_2$ *via* catalysis. The nucleation theory is described as the equation:[111]

$$J = J_0 e^{-\Delta G/k_B T}$$

where $J$ is the nanobubble embryo formation rate, $k_B$ is the Boltzmann constant, $T$ is the temperature. $J_0$ is the nanobubble embryo formation rate when $\Delta G$ equals 0, $\Delta G$ is the free energy of formation of nanobubble embryos, related to the surface curvature:[112]

$$\Delta G=\Delta G_0 f$$

where $\Delta G_0$ is the free energy of homogeneous formation of nanobubble embryos and $f$ is the shape factor determined by the surface curvature. According to nucleation theory, the concave shape reduces the free energy barrier for nanobubble formation on the inner surface. The confined space of the cavity also facilitates $O_2$ accumulation, while rapid diffusion into the bulk solution of $O_2$ on outer surface inhibits bubble growth.[95] Simulations predict that the inner surface can attain dissolved oxygen concentrations up to 120 mmol/L, sufficient for nucleation, while the 12 mmol/L outer surface concentration remains below the nucleation threshold (Fig. 9E).[100] As the nanobubbles generated inside propel outwards through the vase opening, they continuously grow by incorporating newly produced $O_2$ to power directional bubble propulsion. Strategies to optimize bubble motors focus on tailoring speed and directionality by tuning fabrication parameters like catalyst placement/concentration and channel dimensions for bubble flow focusing.[113,114] Cyclic bubble generation can be achieved using biochemical reactions or applied voltage.[115]

Self-thermophoresis can be achieved by creating an asymmetric temperature gradient in the solution around the nanoparticles, resulting in asymmetric pressure. The Au nanoshells can also absorb near-infrared light at *ca.* 808 nm and exhibit a high-light thermal conversion that creates a heterogeneous temperature gradient around the Janus nanomotor, triggering directional propulsion.[116] As shown in Fig. 9F, the thermal gradient of the nanomotors from the Au nanoshell side solution is obviously larger than that from the periodic mesoporous organosilica (PMO) side. Such a thermal gradient can further induce the generating thermophoretic force ($F$) obtained by equation:

$$F=-C\Delta T$$

where variable $C=(9\pi d_p \eta^2 k_a)/(2\rho_g T k_p)$, $d_p$ is the diameter of particles, $\eta$ is the viscosity of fluid, $k_a$ is the thermal conductivity of fluid, $\rho_g$ is the fluid density, $k_p$ is the thermal conductivity of particles (Fig. 9G). Therefore, the thermophoresis force $F$ is proportional to the thermal gradient $\Delta T$, and its direction is opposite to the direction of $\Delta T$. In addition to creating a thermal gradient around the material, thermal volume expansion caused by high temperature can also rapidly increase the liquid pressure in the cavity inside the hollow structure (Fig. 9H).[117] The high pressure in the cavity forces the liquid inside the hollow structure to drain out of the void, creating a net reverse thrust in the void and pushing the motor to move (Fig. 9I). In addition, the self-thermophoresis propulsion mechanism is often combined with other mechanisms, such as self-electrophoresis and self-diffusiophoresis in a motor to achieve multiple transformations of phoretic propulsion by changing external conditions, so as to better regulate its motion behavior.[116,118]

Similar to natural organism, nanoparticles exhibit migration in solute or solvent concentration gradients. Chemotaxis refers to the movement of particles migrating to regions of high solute concentration, while antichemotaxis refers to the movement of particles in the direction of low concentrations. The mechanism of this behavior is thought to be caused by non-specific interactions between particles and solutes or specific active site-substrate binding by diffusion electrophoresis.[119,120] As the asymmetric hollow structures are capable of reorientation in the chemical gradient of the fuel or fuel reaction regulators, the synthesized chemotactic particles sensitive to the chemical signals of $H_2O_2$,[121−123] glucose,[124,125] and $CO_2$[126] have been demonstrated.

For example, Joseph *et al*.[127] investigated a novel chemotactic material, asymmetric polymeric vesicles encapsulated with glucose oxidase and catalase enzymes, which can catalyze the oxidation of glucose to produce *D*-glucono-*δ*-lactone and water. When exposed to a glucose concentration gradient field, the enzymatic reactions inside the vesicles produce products that diffuse out through the more permeable PDPA domain, generating a product concentration gradient field around the vesicle with the function $\Delta c_p = A[\cos(\beta/2)]^{\mathrm{nint}(\frac{2\pi}{\alpha})}$, where $\beta$ is the orientation angle of the vesicle, $\alpha$ is the sector angle of the PBO domain, and $A$ is a proportionality constant, as shown in Fig. 9J. Due to the different permeability of PDPA and PBO regions on the vesicle, the surface slip velocity $v$ is generated as equation, $v = -\mu\Delta c(r_p)$, where $\mu$ is the so-called "electrophoretic mobility" and $\Delta c$ is the projection of the concentration gradient at the position $r_p$ on the surface of the particle.[128] This slip velocity drives the directed motion of the vesicles toward higher concentration regions, realizing chemotaxis. The trajectories of the aggregates show that they are the result of a series of running and redirecting events on a millisecond time scale, so that the aggregates rapidly reorient to the gradient and the ensuing self-propulsion, as shown in Fig. 9K.


https://doi.org/10.1007/s40242-024-4082-9

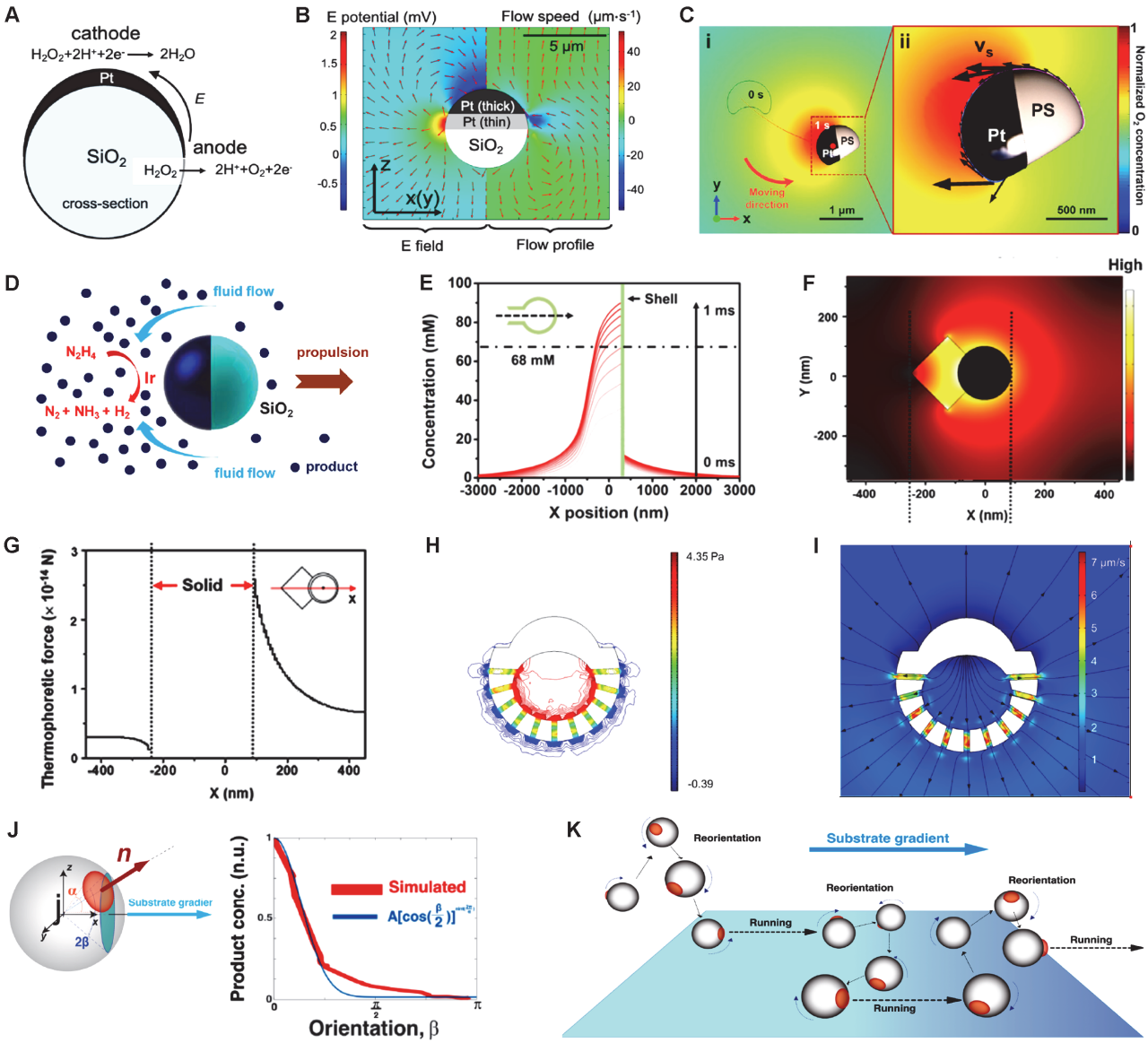


**Fig. 9 Tentative scheme of the operation of self-electrophoresis on a $SiO_2$-Pt micromotor in $H_2O_2$ (A), numerical simulations result of the electrical potential and electric field lines of $SiO_2$-Pt (B), dynamic simulation of the flow field distribution (black lines with a narrow) around the HBJM with the normalized $O_2$ concentration distribution (C), schematic of catalytic Ir/$SiO_2$ Janus micromotors (D), simulated transient concentration distribution of $O_2$ at the symmetric axis (E), illustration of the steady-state thermal gradient distribution of the Janus nanomotor in water under 1.02 W/cm$^2$ NIR irradiation (F), distribution of the thermophoretic force along the central line of the Janus nanomotor (inset) (G), pressure distribution (H) and fluid velocity distribution (I) of the motor at 50 ns, schematics of an asymmetric polymersome and its reference axis (J), and schematic of the proposed mechanisms of asymmetric polymersome chemotaxis, which consists of an alternation of running and reorientation events (K)**

(A, B) Reprinted with permission from Ref. [102], Copyright 2021, American Chemical Society; (C) reprinted with permission from Ref. [108], Copyright 2023, Elsevier; (D) reprinted with permission from Ref. [110], Copyright 2014, American Chemical Society; (E) reprinted with permission from Ref. [100], Copyright 2022, American Chemical Society; (F, G) reprinted with permission from Ref. [116], Copyright 2022, American Chemical Society; (H, I) reprinted with permission from Ref. [117], Copyright 2022, American Chemical Society; (J, K) reprinted with permission from Ref. [127], Copyright 2017, the Authors.

### 3.3 Motion-induced Targeted Release of Anisotropic Hollow Structures

Anisotropic hollow nano/microstructures enable directional movement powered by chemical fuels or light, allowing them to actively carry and deliver drugs. Glucose is the most effective source of necessary metabolic energy, a precursor of biosynthesis and a biochemical signal molecule in living organisms, showing the responsibility of a major pathological index. Glucose as a driving energy source can not only improve the biocompatibility of motors without additional fuel, but also achieve the goal by building a

biochemical reaction to produce a butterfly effect in the organisms. Lee *et al*.[67] reported an "egg-in-nest" structure (Au/Pt-ENs), which exhibited high diffusion and displacements as the result of dual enzyme-relay-like catalytic cascade in glucose. Benefiting from the enhanced motion in glucose, the Au/Pt-ENs with high diffusiophoresis in cell culture containing 100 mmol/L glucose increased the nanomotor-membrane interaction, thereby increasing their cell internalization (Fig. 10A). The hollow structures also facilitate the high-loading encapsulation of enzymes and molecular cargoes and delivery to the living cells, as proven in Fig. 10B. The red fluorescence spots in the cytoplasmic region of the cells treated with the DOX-loaded-Au/Pt-ENs incubated with glucose solutions exhibited a clear increase compared with the control group, due to the enhanced diffusion.

The chemotactic synthetic vesicles towards high glucose sources demonstrated promising functionality for biomedical applications. By encapsulating glucose oxidase and catalase enzymes within asymmetric polymersomes, the vesicles are able to self-propel in glucose gradients, mimicking biological chemotaxis at the nanoscale.[127] This active diffusion property allows the vesicles to autonomously cross the blood-brain barrier and enter the central nervous system when combined with the low-density lipoprotein receptor-related protein 1 (LRP-1) targeting peptide Angiopep-2 (LA). Experiments show the chemotactic vesicles increased brain delivery of polymersomes functionalized with LA across the blood-brain barrier (BBB) in a rat model by 4-fold compared to non-chemotactic controls (Fig. 10C). The immunofluorescence histologies of the brain sections further indicate the vesicles could have improved distribution and effective passage across the BBB due to their propulsion-enhanced transport characteristics (Fig. 10D).

$H_2O_2$ is often used as a fuel for propelling micro and nano engines, because it can decompose to produce $O_2$, where the generated oxygen concentration gradient or oxygen bubbles provide thrust to propel the engine forward.[129−132] Asymmetric $O_2$ bubbles *via* $H_2O_2$ decomposition propelled Janus heparin loaded ammoniated-hollow mesoporous silica (H-A-HMS) show great potential in targeted drug delivery, as the mesoporous structure enables controlled heparin release up to 25 d while maintaining biocompatibility (Fig. 11A).[133] Compared to other non-hollow structures, the hollow architecture

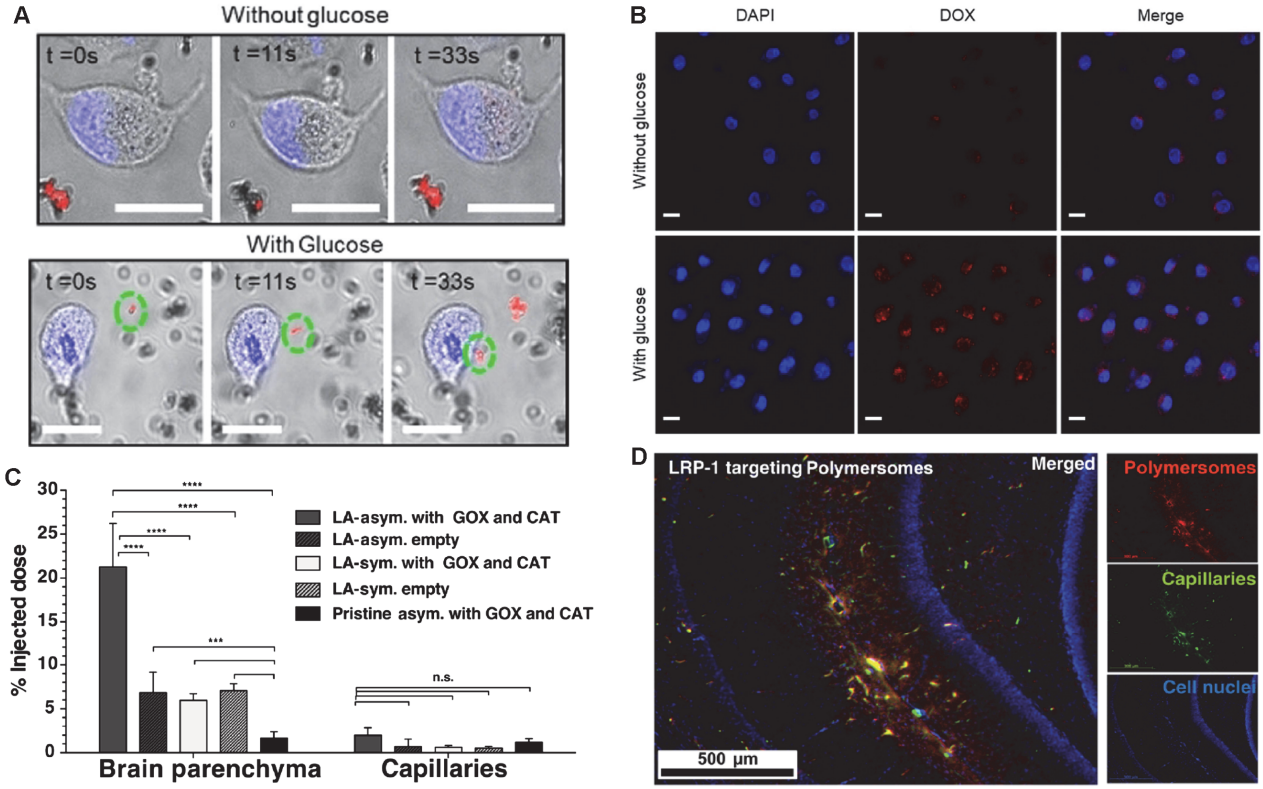


**Fig. 10 Snapshots of a real time monitoring of Rh 110 modified Au/Pt-ENs interaction with MDA-MB cells through CLSM (scale bars= 25 mm) (A), CLSM imaging of MDA-MB cells and doxorubicin after treatment with DOX-loaded-Au/Pt-ENs (scale bars= 25 mm) (B), percentage of the injected dose found in the rat brain parenchyma and the capillary fraction 10 min after carotid artery *in situ* perfusion of samples (C), and immunofluorescence histologies of rat hippocampus sections of animals treated with asymmetric polymersomes loaded with glucose oxidase and catalase (D)**

(A, B) Reprinted with permission from Ref. [67], Copyright 2021, Wiley-VCH; (C, D) reprinted with permission from Ref. [127], Copyright 2017, the Authors.


https://doi.org/10.1007/s40242-024-4082-9

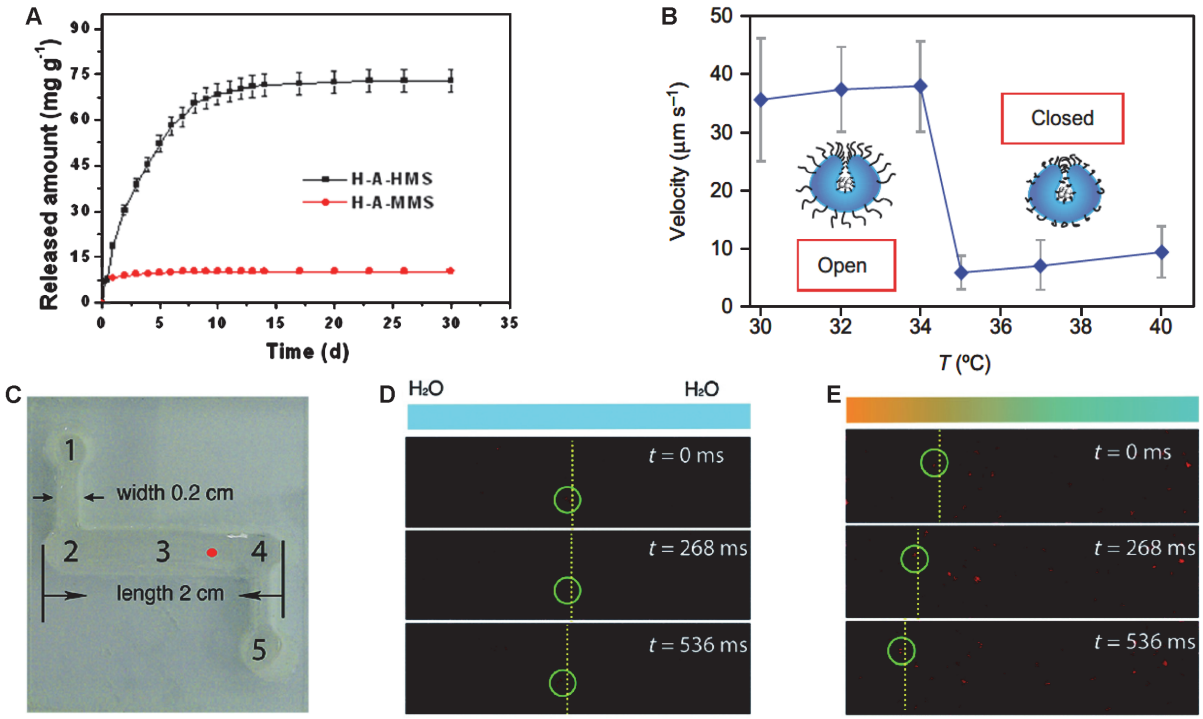


**Fig. 11 Release profiles of heparin on different samples (A), motion of a PtNP-stoma-brush in the presence of $H_2O_2$ at different temperatures (B), glass channel design for chemotaxis evaluation (C), and motion of DOX and PtNP loaded stomatocytes upon addition of $H_2O$ (D) or 0.5% $H_2O_2$ (E) (in the green circles, the movement of a single particle is tracked)**

(A) Reprinted with permission from Ref. [133], Copyright 2018, American Chemical Society; (B) reprinted with permission from Ref. [89], Copyright 2016, Springer Nature; (C—E) reprinted with permission from Ref. [122], Copyright 2015, Wiley-VCH.

endows higher drug loading capacity. The regulation of speed in $H_2O_2$ can be achieved by growing temperature-sensitive polymer brushes on nanomotors.[89] By changing the temperature, the polymer switch can be changed to realize the control of the hydrogen peroxide fuel amount, realizing reversible control over the motion speed without affecting catalytic activity (Fig. 11B). This system displayed potential applications in controllable cargo transportation, as the nanomotors' size and speed can be precisely regulated by an external stimulus.[134]

Feng *et al.*[68] prepared unique hollow-shell microspheres (h-$MnO_2$@Zr-CP) as micromotors fueled by $H_2O_2$ due to the catalase-like enzyme mimicking activities, showing promise in biocatalysis and other fields benefiting from multifunctional micro-/nano-carriers. Composed of polymeric stomatocytes loaded with platinum nanoparticles and doxorubicin, the structures demonstrate autonomous movement in response to $H_2O_2$ gradients.[122] Remarkably, the nanomotors also guide towards higher fuel concentrations, exhibiting chemotaxis towards hydrogen peroxide secreting cells like neutrophils. Motors at position 4 with an average velocity of 15.47 μm/s accelerated to 19.64 μm/s at the red spot position with the addition of 0.5% $H_2O_2$ (Fig. 11C). The net displacement of the nanomotors was also confirmed by observations with microscopy (Fig. 11, D and E). This directed motion holds promise for advanced targeted drug delivery applications, allowing payloads to actively navigate tissues to diseased sites against interstitial pressure gradients. Compared to passively diffusing carriers, these nanomotors may more effectively deliver therapeutics to late-stage tumors.

Light is considered to be one of the most versatile sources to regulate drug release because it achieves photothermal therapy while regulating material movement. For example, the asymmetric porous and hollow carbon nanoparticles (APHC NPs) exhibited superior photothermal ability, and achieve autonomous motion when irradiated with near-infrared (NIR) light, as evidenced by a 70.2% increase in diffusion coefficient from 3.15 μm$^2$/s to 5.36 μm$^2$/s.[117] Upon NIR heating, the APHC NPs loaded with DOX and PCM (DOX-PCM-APHC) exhibited temperature-controlled release of DOX due to the phase transition of PCM (Fig. 12, A and B). Compared with DOX-PCM-APHC without laser irradiation (Fig. 12C), the red fluorescence of DOX appears inside the nucleus under laser irradiation of DOX-PCM-APHC (Fig. 12D). The DOX-PCM-APHC with laser irradiation also shows enhanced anticancer activity, with only 46.4% of the cells surviving, which can be attributed to the synergistic effect arising from photothermal and chemotherapy. Tu *et al.*[135]

synthesized hollow $Cu_2O$ micromotors with a cross-linked polyhedral microstructure, which demonstrated intelligent pH responsive phototaxis, showing great potential for targeted drug delivery (Fig. 12E). It is also possible to integrate photothermal or photocatalytic materials with chemical energy conversion materials in a nanostructure to achieve multiple mechanism propulsion and multi-functional motors. Ma *et al.*[136] synthesized a mesoporous silica coated with half gold nanoshell and photosensitizer 5,10,15,20-tetrakis(4-aminophenyl) porphyrin (TAPP) modification that has several integrated functions. It can achieve self-propulsion in hydrogen peroxide concentrations, which can be accelerated by adding NIR light (Fig. 12F). This active motion allows the nanomotor to serve as an all-in-one theranostic platform for tumor detection, dual-modality fluorescence and photoacoustic imaging, as well as synergistic photothermal and photodynamic cancer therapy both *in vitro* and *in vivo* shown in Fig. 12G. The nanomotor showed superior tumor suppression of about 90.3%, while the passive treatment methods only up to 52.7% (Fig. 12H). The excellent properties are attributed to the autonomous movement of the motors in $H_2O_2$ to enhance the penetration into the tumor's deep sites, the TAPP endowed therapy photodynamic ability for cancer treatment, and the $O_2$ generated by the decomposition of $H_2O_2$ to improve the

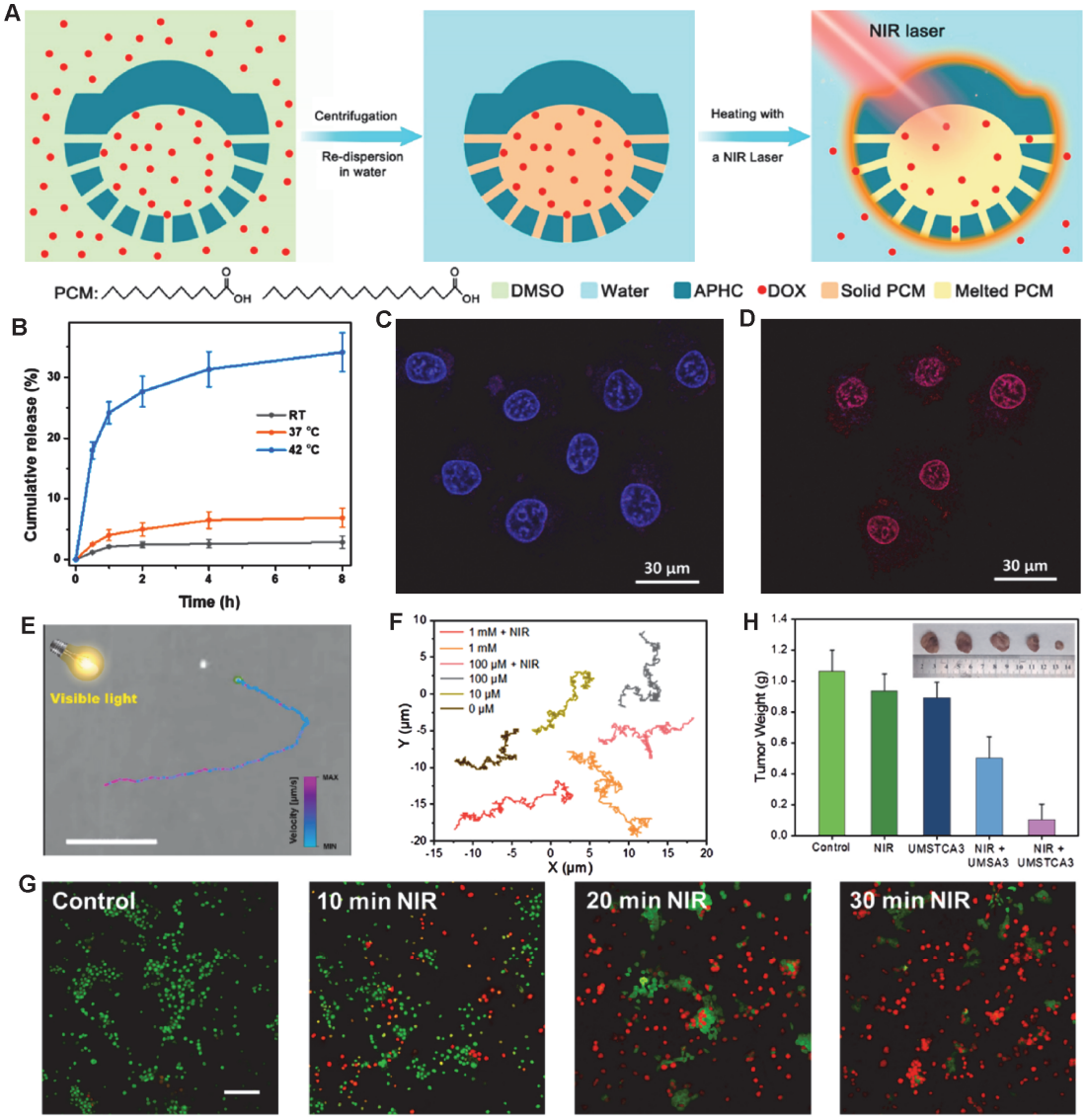


**Fig. 12 Schematic illustration showing the encapsulation and release of PCM and DOX in APHC nanoparticles (A), cumulative DOX release from the APHC nanoparticles (B), fluorescence images of HeLa cells incubated with DOX-PCM-APHC (C) and DOX-PCM-APHC with NIR laser irradiation (D), trajectory of a single $Cu_2O$ micromotor reversing from negative to positive phototaxis under pH gradient (scale bar=100 μm) (E), motion trajectories of motor under different conditions (F), live (green)/dead (red) assays of 4T1 cells treated with nanomotors under NIR light for different exposure time (scale bar=100 μm) (G), and tumor weights after 20 d of different treatments (H)**

(A—D) Reprinted with permission from Ref. [117], Copyright 2022, American Chemical Society; (E) reprinted with permission from Ref. [135], Copyright 2022, Elsevier; (F—H) reprinted with permission from Ref. [136], Copyright 2022, Elsevier.


https://doi.org/10.1007/s40242-024-4082-9

photodynamic ability.

## 4 Conclusions and Outlook

To develop more personalized and and programmable drug delivery systems, coordinated regulation of carrier properties from the molecular to macroscale levels is required. At the molecular level of interactions between drugs and carries, modulation of multi-hierarchical structures can enable distinct interaction forces within different spatial domains of carriers, thereby facilitating sequential and responsive drug release in response to microenvironmental cues. At the nanomicro level of carrier force, regulation of asymmetric three-dimensional structures in materials allows carriers to construct asymmetric force fields to achieve directed motion and interface fluid flow. It can sense targeted environmental signals and constantly regulate the direction and speed of movement, so as to achieve the targeted transport and release of drugs.

While multil-founctional hollow structures-based delivery platforms have demonstrated enhanced therapeutic effects in preliminary studies, significant challenges remain to be addressed before clinical translation. Rational design of complex multi-functional hollow structures remains difficult due to limitations in current synthesis capabilities. Artificial intelligence and big data analysis can be utilized to summarize the structural and internal microenvironment requirements of efficient drug delivery systems, and clarify the influence regulations of carrier structure and inner microenvironment on drug loading, delivery and release, helping guide computational design of optimized hollow architectures.

Controllable and precise synthesis and functionalization methods also need advancement to program drug release profiles. By combining computation and experiments, concentration wave modulation can enable precise synthesis of hollow multishell structures. Exploring assembly or reaction mechanisms at interfaces may provide new pathways and shed light on diffusion control within restricted spaces.

Mechanistic studies of drug transport behaviors within confined spaces of multil-founctional hollow carriers are equally important. The impacts of carrier structure on drug molecular aggragate behaviors require clarification. Deciphering the drug loading and release kinetics models in multishells and the influence of structure on transport behaviors would offer insights for structural design of more programmable and intelligent drug delivery. Clarifying the relation between structure and performance on the surface-functionalization of HoMS may reveal regulatory principles to enhance targeted delivery.

Moving forward, multidisciplinary research integrating computational modeling, precise synthesis and characterization techniques are necessary to address these challenges and accelerate clinical translation of intelligent multi-functional hollow carriers. With continous progress, the HoMS would be a platform that plays a key role in developing personalized precision medicine by enabling combination therapies, targeted delivery and real-time treatment monitoring for a better life.

## Acknowledgements

This work was supported by the National Natural Science Foundation of China (Nos. 92163209, 21821005 and 51932001), and the Beijing Natural Science Foundation, China (No. JQ22004).

## Conflicts of Interest

WANG Dan is an editorial board member for Chemical Research in Chinese Universities. YANG Nailiang is a youth executive editorial board member for Chemical Research in Chinese Universities. They were not involved in the editorial review or the decision to publish this article. The authors declare no conflicts of interest.

## References

[1] Duan L., Yang L., Jin J., Yang F., Liu D., Hu K., Wang Q., Yue Y., Gu N., *Theranostics*, **2020**, *10*, 462.
[2] Sanjay S. T., Zhou W., Dou M., Tavakoli H., Ma L., Xu F., Li X., *Adv. Drug. Deliv. Rev.*, **2018**, *128*, 3.
[3] Han L., Zheng Y., Luo H., Feng J., Engstler R., Xue L., Jing G., Deng X., Del Campo A., Cui J., *Angew. Chem. Int. Ed.*, **2020**, *59*, 5611.
[4] Yuan M. W., Shi S. L., Luo Y. P., Yu Y., Wang S. H., Chen C., *Chem. Res. Chinese Universities*, **2022**, *38*, 999.
[5] Yan T., He J., Liu R., Liu Z., Cheng J., *Carbohydr. Polym.*, **2020**, *231*, 115706.
[6] van der Meel R., Sulheim E., Shi Y., Kiessling F., Mulder W. J. M., Lammers T., *Nat. Nanotechnol.*, **2019**, *14*, 1007.
[7] Liu Q., Xu N., Liu L., Li J., Zhang Y., Shen C., Shezad K., Zhang L., Zhu J., Tao J., *ACS Appl. Mater. Interfaces*, **2017**, *9*, 21673.
[8] Li L., Liu T., Fu C., Meng X., Liu H., *J. Nanosci. Nanotechnol.*, **2016**, *16*, 6766.
[9] Yang G., Xu L., Xu J., Zhang R., Song G., Chao Y., Feng L., Han F., Dong Z., Li B., Liu Z., *Nano Lett.*, **2018**, *18*, 2475.
[10] Qiao Y., Wan J., Zhou L., Ma W., Yang Y., Luo W., Yu Z., Wang H., *Nanobiotechnol.*, **2019**, *11*, e1527.
[11] Wu J., Ma G., *J. Control. Release*, **2019**, *303*, 101.
[12] Wang J., Wan J., Yang N., Li Q., Wang D., *Nat. Rev. Chem.*, **2020**, *4*, 159.
[13] Wang J., Wan J., Wang D., *Acc. Chem. Res.*, **2019**, *52*, 2169.
[14] Wang Z., Qi J., Yang N., Yu R., Wang D., *Mater. Chem. Front.*, **2021**, *5*, 1126.
[15] Wang L., Wan J., Wang J., Wang D., *Small Struct.*, **2020**, *2*, 2000041.
[16] Zhao X. L., Yang M., Wang J. Y., Wang D., *Chem. Res. Chinese Universities*, **2023**, *39*, 630.
[17] Han W. S., Wang Y. L., Wan J. W., Wang D., *Chem. Res. Chinese Universities*, **2022**, *38*, 117.
[18] Ge W. J., Chen X. C., Ma R. Z., Zheng S. Y., Shang N. Z., Zhao X. X., *Chem. Res. Chinese Universities*, **2024**, *40*, 437.
[19] Hortelão A. C., Patiño T., Perez-Jiménez A., Blanco À., Sánchez S., *Adv. Funct. Mater.*, **2018**, *28*, 1705086.
[20] Chen H., Li T., Liu Z., Tang S., Tong J., Tao Y., Zhao Z., Li N., Mao C., Shen J., Wan M., *Nat. Commun.*, **2023**, *14*, 941.
[21] Kwak M., Jung I., Kang Y. G., Lee D. K., Park S., *Nanoscale*, **2018**,

*10*, 18690.
[22] Xu X., Kim K., Fan D., *Angew. Chem. Int. Ed.*, **2015**, *54*, 2525.
[23] Nie C. P., Ma T. R., Chen T. T., Chu X., *Chem. Res. Chinese Universities*, **2024**, *40*, 333.
[24] Fusi A. D., Li Y., Llopis A., Patiño T., van Hest J. C. M., Abdelmohsen L. K. E. A., *Angew. Chem. Int. Ed.*, **2022**, *62*, e202214754.
[25] Qiu J., Xu J., Xia Y., *Adv. Healthc. Mater.*, **2021**, *10*, e2000587.
[26] Fu J., An D., Song Y., Wang C., Qiu M., Zhang H., *Coordination Chem. Rev.*, **2020**, *422*, *213467*.
[27] Noriaki S., *Mater. Chem. Phys.*, **2004**, *88*, 235
[28] Li Z., Lai X., Wang H., Mao D., Wang D., *J. Phys. Chem. C*, **2009**, *113*, 2792
[29] Wang J., Cui Y., Wang D., *Nanoscale Horiz.*, **2020**, *5*, 1287.
[30] Zhao X., Wang J., Yu R., Wang D., *J. Am. Chem. Soc.*, **2018**, *140*, 17114.
[31] Zhao X., Yu R., Tang H., Mao D., Qi J., Wang B., Zhang Y., Zhao H., Hu W., Wang D., *Adv. Mater.*, **2017**, *29*, 1700550.
[32] Dong Z., Ren H., Hessel C. M., Wang J., Yu R., Jin Q., Yang M., Hu Z., Chen Y., Tang Z., Zhao H., Wang D., *Adv. Mater.*, **2014**, *26*, 905.
[33] Dong Z., Lai X., Halpert J. E., Yang N., Yi L., Zhai J., Wang D., Tang Z., Jiang L., *Adv. Mater.*, **2012**, *24*, 1046.
[34] Salhabi E. H. M., Zhao J., Wang J., Yang M., Wang B., Wang D., *Angew. Chem. Int. Ed.*, **2019**, *58*, 9078.
[35] Bi R., Xu N., Ren H., Yang N., Sun Y., Cao A., Yu R., Wang D., *Angew. Chem. Int. Ed.*, **2020**, *59*, 4865.
[36] You F., Wan J., Qi J., Mao D., Yang N., Zhang Q., Gu L., Wang D., *Angew. Chem. Int. Ed.*, **2019**, *59*, 721.
[37] Zhang J., Wan J., Wang J., Ren H., Yu R., Gu L., Liu Y., Feng S., Wang D., *Angew. Chem. Int. Ed.*, **2019**, *58*, 5266.
[38] Hou P., Li D., Yang N., Wan J., Zhang C., Zhang X., Jiang H., Zhang Q., Gu L., Wang D., *Angew. Chem. Int. Ed.*, **2021**, *60*, 6926.
[39] Wang H., Qi J., Yang N., Cui W., Wang J., Li Q., Zhang Q., Yu X., Gu L., Li J., Yu R., Huang K., Song S., Feng S., Wang D., *Angew. Chem. Int. Ed.*, **2020**, *59*, 19691.
[40] Wei Y., Cheng Y., Zhao D., Feng Y., Wei P., Wang J., Ge W., Wang D., *Angew. Chem. Int. Ed.*, **2023**, *62*, e202302621.
[41] Wang W., Zheng T., Zhang M., Zhang Q., Wu F., Liu Y., Zhang L., Zhang J., Wang M., Sun Y., *Biomate. Sci.*, **2020**, *8*, 1748.
[42] Li Z., Xu K., Qin L., Zhao D., Yang N., Wang D., Yang Y., *Adv. Mater.*, **2023**, *35*, 2203890.
[43] Ma X., Zhang X., Yang L., Wang G., Jiang K., Wu G., Cui W., Wei Z., *Nanoscale*, **2016**, *8*, 8687.
[44] Conley B. M., Pongkulapa T., Lee K.-B., *Chem*, **2020**, *6*, 2875.
[45] Gao Y., Ji X., He X., Yin Q., Zhang Z., Shi J., Li Y., *ACS Nano*, **2011**, *5*, 9788.
[46] Yang Y., Lu Y., Abbaraju P. L., Zhang J., Zhang M., Xiang G., Yu C., *Angew. Chem. Int. Ed.*, **2017**, *56*, 8446.
[47] Xia Y., Na X., Wu J., Ma G., *Adv. Mater.*, **2019**, *31*, e1801159.
[48] Wang D., *Adv. Mater.*, **2019**, *31*, e1904886.
[49] Zhao D., Yang N., Wei Y., Jin Q., Wang Y., He H., Yang Y., Han B., Zhang S., Wang D., *Nat. Commun.*, **2020**, *11*, 4450.
[50] Liu D., Wan J., Pang G., Tang Z., *Adv. Mater.*, **2019**, *31*, e1803291.
[51] Yang G., Xu L., Chao Y., Xu J., Sun X., Wu Y., Peng R., Liu Z., *Nat. Commun.*, **2017**, *8*, 902.
[52] Fulda S., Galluzzi L., Kroemer G., *Nat. Rev. Drug. Discov.*, **2010**, *9*, 447.
[53] Tan S., Long Y., Han Q., Guan H., Liang Q., Ding M., *ACS Biomate. Sci. Engineer.*, **2020**, *6*, 1387.
[54] Zhao D., Wei Y., Jin Q., Yang N., Yang Y., Wang D., *Angew. Chem. Int. Ed.*, **2022**, *61*, e202206807.
[55] Hao N., Nie Y., Zhang J. X. J., *Micropor. Mesopor. Mater.*, **2018**, *261*, 144.
[56] Ma X., Zhang X., Yang L., Wang G., Jiang K., Wu G., Cui W., Wei Z., *Nanoscale*, **2016**, *8*, 8687.
[57] Cheng K., Sun Z., Zhou Y., Zhong H., Kong X., Xia P., Guo Z., Chen Q., *Biomater. Sci.*, **2013**, *1*, 965.
[58] Soares S. F., Fernandes T., Daniel-da-Silva A. L., Trindade T., *Proc. Math. Phys. Eng. Sci.*, **2019**, *475*, 20180677.
[59] Zhou Y., Han Y., Li G., Yang S., Xiong F., Chu F., *Nanomaterials*, **2019**, *9*, 188.
[60] Huang C. C., Huang W., Yeh C. S., *Biomaterials*, **2011**, *32*, 556.
[61] Yu L., Yu X. Y., Lou X. W., *Adv. Mater.*, **2018**, *30*, 1800939.
[62] Wu X., Si Y. S., Zou Y. B., Mao Y. T., Li Q. J., Zhou S. X., Chen M., Wu L. M., *ACS Appl. Mater. Interfaces*, **2018**, *10*, 31664.
[63] Wang Z. H., Qiu T., Guo L. H., Ye J., He L. F., Li X. Y., *Chem. Eng. J.*, **2019**, *357*, 348.
[64] Bentz K. C., Savin D. A., *Poly. Chem.*, **2018**, *9*, 2059.
[65] Qiu J., Huo D., Xue J., Zhu G., Liu H., Xia Y., *Angew. Chem. Int. Ed.*, **2019**, *58*, 10606.
[66] Arqué X., Romero-Rivera A., Feixas F., Patiño T., Osuna S., Sánchez S., *Nat. Comm.*, **2019**, *10*, 2826.
[67] Kwon T., Kumari N., Kumar A., Lim J., Son C. Y., Lee I. S., *Angew. Chem. Int. Ed.*, **2021**, *60*, 17579.
[68] Sun J., Fu Y., Li R., Feng W., *Chem. Mater.*, **2018**, *30*, 1625.
[69] Xu J., Ma A., Xu Z., Liu X., Chu D., Xu H., *J. Phy. Chem. C*, **2015**, *119*, 28055.
[70] Xu D., Zhou C., Zhan C., Wang Y., You Y., Pan X., Jiao J., Zhang R., Dong Z., Wang W., Ma X., *Adv. Func. Mater.*, **2019**, *29*, 1807727.
[71] Hyun D. C., Lu P., Choi S. I., Jeong U., Xia Y., *Angew. Chem. Int. Ed.*, **2013**, *52*, 10468.
[72] Guan B. Y., Yu L., Lou X. W., *Adv. Sci.*, **2017**, *4*, 1700247.
[73] Zhang Y., Chen J.-J., Zhang G.-H., Chen B.-X., Yan H.-S., *Chinese J. Poly. Sci.*, **2012**, *31*, 294.
[74] Hyuk Im S., Jeong U., Xia Y., *Nat. Mater.*, **2005**, *4*, 671.
[75] Xiong F., Han Y., Wang S., Li G., Qin T., Chen Y., Chu F., *ACS Sustain. Chem. Eng.*, **2017**, *5*, 2273.
[76] Ortiz-Rivera I., Mathesh M., Wilson D. A., *Acc. Chem. Res.*, **2018**, *51*, 1891.
[77] Cai L., Wang H., Yu Y., Bian F., Wang Y., Shi K., Ye F., Zhao Y., *Nat. Sci. Rev.*, **2020**, *7*, 644.
[78] Wilson D. A., Nolte R. J., van Hest J. C., *Nat. Chem.*, **2012**, *4*, 268.
[79] Wilson D. A., Nolte R. J. M., van Hest J. C. M., *J. Am. Chem. Soc.*, **2012**, *134*, 9894.
[80] Abdelmohsen L. K., Nijemeisland M., Pawar G. M., Janssen G. J., Nolte R. J., van Hest J. C., Wilson D. A., *ACS Nano*, **2016**, *10*, 2652.
[81] Adawy A., Amghouz Z., van Hest J. C. M., Wilson D. A., *Small*, **2017**, *13*, 1700642.
[82] Kim K. T., Zhu J. H., Meeuwissen S. A., Cornelissen J. J. L. M., Pochan D. J., Nolte R. J. M., van Hest J. C. M., *J. Am. Chem. Soc.*, **2010**, *132*, 12522.
[83] Tu Y., Peng F., André A. A. M., Men Y., Srinivas M., Wilson D. A., *ACS Nano*, **2017**, *11*, 1957.
[84] Tu Y., Peng F., White P. B., Wilson D. A., *Angew. Chem. Int. Ed.*, **2017**, *56*, 7620.
[85] Shao J., Cao S., Che H., De Martino M. T., Wu H., Abdelmohsen L., van Hest J. C. M., *J. Am. Chem. Soc.*, **2022**, *144*, 11246.
[86] Peng F., Tu Y., Men Y., van Hest J. C. M., Wilson D. A., *Adv. Mat.*, **2016**, *29*, 1604996.
[87] Mathesh M., Sun J., van der Sandt F., Wilson D. A., *Nanoscale*, **2020**, *12*, 22495.
[88] Shao J., Pijpers I. A. B., Cao S., Williams D. S., Yan X., Li J., Abdelmohsen L. K. E. A., van Hest J. C. M., *Adv. Sci.*, **2019**, *6*, 1801678.
[89] Tu Y., Peng F., Sui X., Men Y., White P. B., van Hest J. C. M., Wilson D. A., *Nat. Chem.*, **2017**, *9*, 480.
[90] Toebes B. J., Cao F., Wilson D. A., *Nat. Commun.*, **2019**, *10*, 5308.
[91] Park S. H., Kim J., Lee W.-E., Byun D.J., Kim M. H., *Langmuir*, **2017**, *33*, 2275.
[92] Kim D. H., Woo H.-C., Kim M. H., *Langmuir*, **2019**, *35*, 13700.
[93] Liang J., Kong J., Zhang J., *Chem. Electro. Chem.*, **2021**, *8*, 172.
[94] Yi D. L., Zhang Q., Liu Y. H., Song J. Y., Tang Y., Caruso F., Wang Y. J., *Angew. Chem. Int. Ed.*, **2016**, *55*, 14733.

[95] Qiu B. l., Xie L., Zeng J., Liu T. Y., Yan M., Zhou S., Liang Q. R., Tang J. Y., Liang K., Kong B., *Adv. Funct. Mater.*, **2021**, *31*, 2010694.
[96] Jiang S., Kaltbeitzel A., Hu M., Suraeva O., Crespy D., Landfester K., *ACS Nano*, **2019**, *14*, 498.
[97] Chen C. H., Wang H. Y., Han C. L., Deng J., Wang J., Li M. M., Tang M. H., Jin H. Y., Wang Y., *J. Am. Chem. Soc.*, **2017**, *139*, 2657.
[98] Gao C., Zhou C., Lin Z., Yang M., He Q., *ACS Nano*, **2019**, *13*, 12758.
[99] Zhou C., Gao C., Wu Y., Si T., Yang M., He Q., *Angew. Chem. Int. Ed.*, **2022**, *61*, e202116013.
[100] Liu T., Xie L., Zeng J., Yan M., Qiu B., Wang X., Zhou S., Zhang X., Zeng H., Liang Q., He Y., Liang K., Liu J., Velliou E., Jiang L., Kong B., *ACS Appl. Mater. Interfaces*, **2022**, *14*, 15517.
[101] Dey K. K., Sen A., *J. Am. Chem. Soc.*, **2017**, *13*, 7666.
[102] Lyu X., Liu X., Zhou C., Duan S., Xu P., Dai J., Chen X., Peng Y., Cui D., Tang J., Ma X., Wang W., *J. Am. Chem. Soc.*, **2021**, *143*, 12154.
[103] Paxton W. F., Baker P. T., Kline T. R., Wang Y., Mallouk T. E., Sen A., *J. Am. Chem. Soc.*, **2006**, *128*, 14881.
[104] Jun I. K., Hess H., *Adv. Mater.*, **2010**, *22*, 4823.
[105] Paxton W. F., Kistler K. C., Olmeda C. C., Sen A., St Angelo S. K., Cao Y., Mallouk T. E., Lammert P. E., Crespi V. H., *J. Am. Chem. Soc.*, **2004**, *126*, 13424.
[106] Anderson J. L., Lowell. M. E., Prieve. D. C., *J. Fluid Mech.*, **1982**, *117*, 107.
[107] Zhang Y. F., Hess H., *Nat. Rev. Chem.*, **2021**, *5*, 500.
[108] Xiong K., Lin J., Chen Q., Gao T., Xu L., Guan J., *Matter*, **2023**, *6*, 907.
[109] Prieve. D. C, Ebel. J. P., Lowell. M. E., *J. Fluid. Mech.*, **1984**, *148*, 247.
[110] Gao W., Pei A., Dong R., Wang J., *J. Am. Chem. Soc.*, **2014**, *136*, 2276.
[111] Huang W., Manjare M., Zhao Y., *J. Phy. Chem. C*, **2013**, *117*, 21590.
[112] Fletcher N. H., *J. Chem. Phy.*, **1958**, *29*, 572.
[113] Nourhani A., Karshalev E., Soto F., Wang J., *Research*, **2020**, *2020*, 7823615.
[114] Ma X., Hortelao A. C., Miguel-Lopez A., Sanchez S., *J. Am. Chem. Soc.*, **2016**, *138*, 13782.
[115] Wang T., Zheng M., Wang L., Ji L., Wang S., *Nanotechnology*, **2020**, *31*, 355504.
[116] Liu M., Chen L., Zhao Z., Liu M., Zhao T., Ma Y., Zhou Q., Ibrahim Y. S., Elzatahry A. A., Li X., Zhao D., *J. Am. Chem. Soc.*, **2022**, *144*, 3892.
[117] Xie L., Yan M., Liu T., Gong K., Luo X., Qiu B., Zeng J., Liang Q., Zhou S., He Y., Zhang W., Jiang Y., Yu Y., Tang J., Liang K., Zhao D., Kong B., *J. Am. Chem. Soc.*, **2022**, *144*, 1634.
[118] Xing Y., Zhou M., Xu T., *Angew. Chem. Int. Ed.*, **2020**, *59*, 1436.
[119] Agudo-Canalejo J., Illien P., Golestanian R., *Nano Lett.*, **2018**, *18*, 2711.
[120] Schurr J. M., Fujimoto B. S., Huynh L., Chiu D. T., *J. Phy. Chem. B*, **2013**, *117*, 7626.
[121] Baraban L., Harazim S. M., Sanchez S., Schmidt O. G., *Angew. Chem. Int. Ed.*, **2013**, *52*, 5552.
[122] Peng F., Tu Y., van Hest J. C. M., Wilson D. A., *Angew. Chem. Int. Ed.*, **2015**, *54*, 11662.
[123] Ma X., Hahn K., Sanchez S., *J. Am. Chem. Soc.*, **2015**, *137*, 4976.
[124] Ji Y., Lin X., Wu Z., Wu Y., Gao W., He Q., *Angew. Chem. Int. Ed.*, **2019**, *58*, 12200.
[125] Zhou C., Gao C., Wu Y., Si T., Yang M., He Q., *Angew. Chem. Int. Ed.*, **2022**, *61*, 355504.
[126] Mou F., Xie Q., Liu J., Che S., Bahmane L., You M., Guan J., *Nat. Sci. Rev.*, **2021**, *8*, nwab066.
[127] Joseph A., Claudia Contini C., Denis Cecchin D., Sophie Nyberg S., Ruiz-Perez L., Gaitzsch J., Fullstone G.,Tian X., Battaglia G., *Sci. Adv.*, **2017**, *3*, e1700362.
[128] Popescu M. N., Uspal W. E., Bechinger C., Fischer P., *Nano Lett.*, **2018**, *18*, 5345.
[129] Liebchen B., Lowen H., *Acc. Chem. Res.*, **2018**, *51*, 2982.
[130] Mathesh M., Sun J., Wilson D. A., *J. Mater. Chem. B*, **2020**, *8*, 7319.
[131] Mathesh M., Bhattarai E., Yang W., *Angew. Chem. Int. Ed.*, **2022**, *61*, e202113801.
[132] Liu T., Xie L., Price C. H., Liu J., He Q., Kong B., *Chem. Soc. Rev.*, **2022**, *51*, 10083.
[133] Hu S., Shao S., Chen H., Sun J., Zhai J., Zheng H., Wan M., Liu Y., Mao C., Zhao J., *J. Phy. Chem. C*, **2018**, *122*, 9680.
[134] Ma X., Jang S., Popescu M. N., Uspal W. E., Miguel-Lopez A., Hahn K., Kim D. P., Sanchez S., *ACS Nano*, **2016**, *10*, 8751.
[135] Tan H., Chen B., Liu M., Jiang J., Ou J., Liu L., Wang F., Ye Y., Gao J., Sun J., Peng F., Tu Y., *Chem. Eng. J.*, **2022**, *448*, 137689.
[136] Chen S., Sun X., Fu M., Liu X., Pang S., You Y., Liu X., Wang Y., Yan X., Ma X., *Biomaterials*, **2022**, *288*, 121744.